RESEARCH ARTICLE

Island Arc WILEY

The δ^{13}C–δ^{18}O variations in marble in the Hida Belt, Japan

Hironobu Harada[1] | Tatsuki Tsujimori[1,2] | Keitaro Kunugiza[3] |
Katsuyuki Yamashita[4] | Shogo Aoki[5,6] | Kazumasa Aoki[5] |
Hideko Takayanagi[1] | Yasufumi Iryu[1]

[1]Graduate School of Science, Tohoku University, Sendai, Japan

[2]Center for Northeast Asian Studies, Tohoku University, Sendai, Japan

[3]Faculty of Human Development, University of Toyama, Toyama, Japan

[4]Graduate School of Natural Science and Technology, Okayama University, Okayama, Japan

[5]Center for Fundamental Education, Okayama University of Science, Okayama, Japan

[6]Graduate School of International Resource Sciences, Akita University, Akita, Japan

Correspondence
Hironobu Harada, Graduate School of Science, Tohoku University, 41 Kawauchi, Aoba-ku, Sendai, Miyagi 980-8576, Japan.
Email: hironobu.harada.s7@dc.tohoku.ac.jp

Abstract

Marble has a great potential to understand a history of various geological events occurring during tectonic processes. In order to decode metamorphic–metasomatic records on C–O isotope compositions of marble at mid-crustal conditions, we conducted a C–O–Sr isotope study on upper amphibolite-facies marbles and a carbonate–silicate rock from the Hida Belt, which was once a part of the crustal basement of the East Asian continental margin. Carbon and oxygen isotope analyses of calcite from marbles (Kamioka area) and a carbonate–silicate rock (Wadagawa area) show a large variation of δ^{13}C [VPDB] and δ^{18}O [VSMOW] values (from −4.4 to +4.2 ‰ and +1.6 to +20.8 ‰, respectively). The low δ^{13}C values of calcites from the carbonate–silicate rock (from −4.4 to −2.9 ‰) can be explained by decarbonation (CO_2 releasing) reactions; carbon–oxygen isotope modeling suggests that a decrease of δ^{13}C strongly depends on the amount of silicate reacting with carbonates. The occurrence of metamorphic clinopyroxene in marbles indicates that all samples have been affected by decarbonation reactions. All δ^{18}O values of calcites are remarkably lower than the marine-carbonate values. The large δ^{18}O variation can be explained by the isotope exchange via interactions between marble, external fluids, and/or silicates. Remarkably low δ^{18}O values of marbles that are lower than mantle value (∼+5 ‰) suggest the interaction with meteoric water at a later stage. Sr isotope ratios (^{87}Sr/^{86}Sr = 0.707255–0.708220) might be close to their protolith values. One zircon associated with wollastonite in a marble thin-section yields a U–Pb age of 222 ± 3 Ma, which represents the timing of the recrystallization of marble, triggered by H_2O-rich fluid infiltration at a relatively high-temperature condition. Our isotope study implies that the upper amphibolite-facies condition, like the Hida Belt, might be appropriate to cause decarbonation reactions which can modify original isotope compositions of marble if carbonates react with silicates.

KEYWORDS
carbon isotope, decarbonation reaction, Hida Belt, marble, oxygen isotope, strontium isotope, zircon U–Pb age

1 | INTRODUCTION

Sedimentary carbonate-rich rocks are often found in a continental platform, and the metamorphosed equivalents occur as lenses and discontinuous layers of marble in various orogenic belts since the early Archean (e.g., Yoshida et al., 2021). Tectono-metamorphic and metasomatic processes in orogens change not only textures, mineral assemblages and chemical compositions, but also the isotope compositions of marble (e.g., Castelli, 1991; Kato et al., 1997; Liu et al., 2015; Ogasawara et al., 2000; Omori et al., 1998; Proyer et al., 2008; Schumacher et al., 2008; Tang et al., 2006; Wan et al., 2020). Hence, the geological, petrological, and geochemical records of marble can be used as a reliable proxy of carbonate-involved processes such as carbonate–silicate–fluid interaction, metamorphic decarbonation, fluid-mediated mineral dissolution, and reprecipitation of carbonate minerals.

In general, sedimentary carbonate (or carbonate-dominant) rocks are divided into seamount carbonate and continental platform carbonate (cf., Ernst, 1974; Liou et al., 2004; Maruyama et al., 1996). The former represents fossilized coral reefs consisting mainly of a nearly pure limestone. On the other hand, the latter one is thick calcareous deposits at a continental platform area; it generally contains a certain amount of terrigenous sedimentary components, typically silicate minerals. In either case, sub-solidus reactions between carbonates and silicates play an important role in CO_2 behaviors in crustal rocks. It has been well known that stable carbon and oxygen isotope compositions of rocks change systematically with decarbonation reactions (e.g., Rumble, 1982; Valley, 1986). Stable C–O isotope studies on marble have been conducted in various metamorphic terranes. Some eclogite-facies marbles from the Sulu-Dabie Terrane, China, preserve the C–O isotope compositions of their protoliths (Rumble et al., 2000). In contrast, the C–O isotope compositions of diamond-bearing dolomite marbles of the Kokchetav Massif, Kazakhstan, have been modified by the fluid alteration during their exhumation (Ohta et al., 2003). The C–O isotope evidence of granulite-facies marbles from the Lützow-Holm Complex, East Antarctica, shows the fluid–rock interactions in various stages of regional metamorphism (Satish-Kumar et al., 2010). In contact metamorphic aureoles, many C–O isotope studies of marble have been performed to understand the systematics of decarbonation reactions during skarn formations and its fluid–rock interactions (e.g., Bickle & Baker, 1990; Gerdes et al., 1995; Nabelek et al., 1984; Nabelek & Morgan, 2012; Roselle et al., 1999).

In this study, we investigated C–O–Sr isotope variations of upper amphibolite-facies marbles and a carbonate–silicate rock from the Hida Belt (Figures 1 and 2). The Hida marble records a Permo-Triassic tectono-metamorphic evolution at a mid-crustal condition (e.g., Jin & Ishiwatari, 1997; Suzuki et al., 1989). Based on C–O–Sr isotope analyses, we show isotope variations and trends with geochemical and geological interpretations. Our new
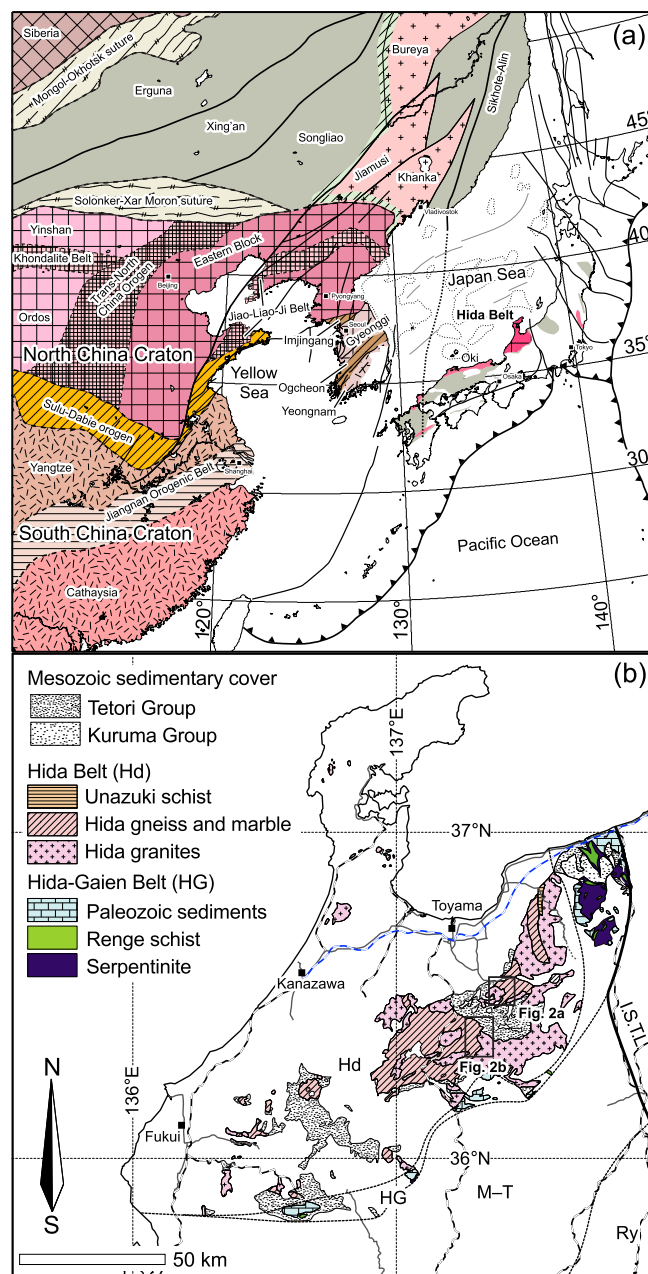
FIGURE 1 (a) Tectonic framework of East Asia. Gray areas are pre-Jurassic accretionary complexes in Japan. Banks and plateaus (surrounded by a dotted line), and spreading axes (gray lines) of the Japan Sea are also shown. The map is modified after Tsujimori and Liou (2005) with compilations of maps proposed by Baba and Yoshida (2020), Isozaki (2019), Khanchuk et al. (2016), Xu et al. (2014), Yanai et al. (2010), Yao et al. (2019), Zhai et al. (2019), Zhang et al. (2020), Zhao et al. (2005), Zhao et al. (2001), and Zhou and Li (2017). (b) Simplified geological map of the Hokuriku region, showing locations of the Kamioka area and the Wadagawa area (modified after Tsujimori, 2002). Hd, Hida Belt; HG, Hida-Gaien Belt; I.S.T.L., Itoigawa–Shizuoka Tectonic Line; M–T, Mino–Tamba Belt; Ry, Ryoke Belt

data aim to contribute to the understanding of crustal evolution of the Hida Belt, as well as, the East Asian continental margin during the Permo-Triassic period.

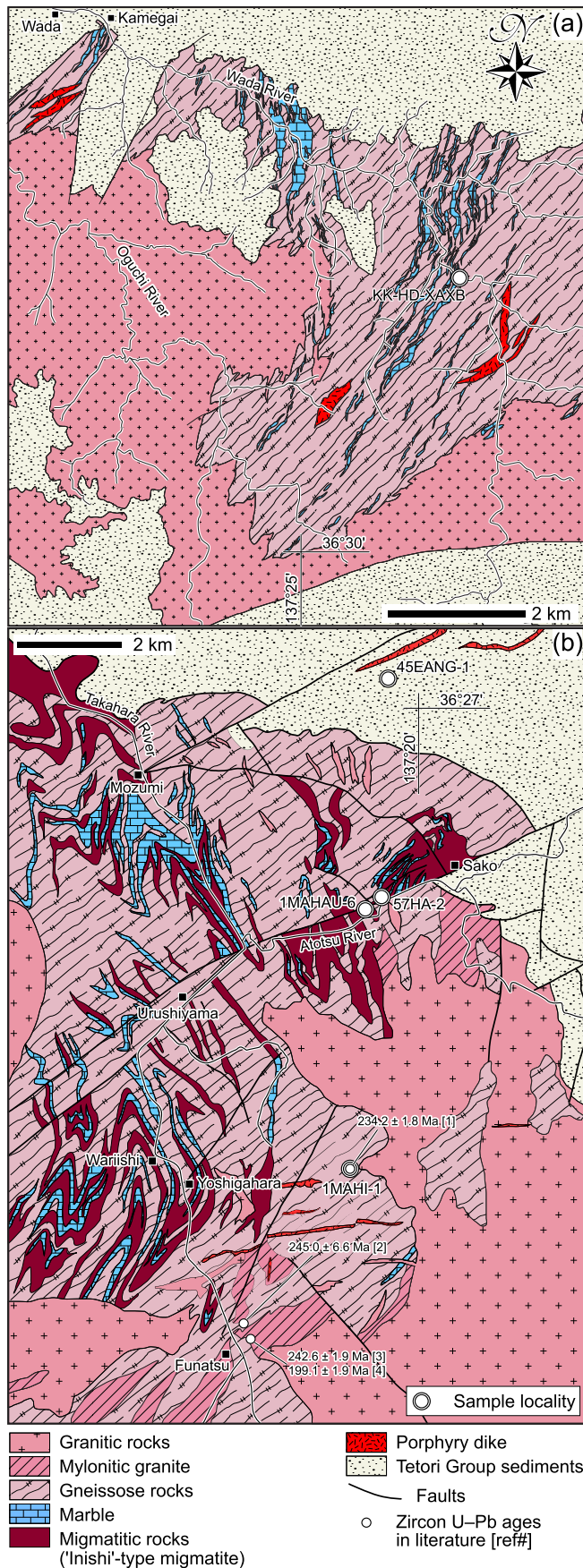**FIGURE 2** (a) A geological map of the Wadagawa area showing a sample locality (modified after Suwa et al., 1981). (b) A geological map of the Kamioka area, showing sample localities (modified after Sakurai et al., 1993). Zircon U–Pb ages showing together with reference: [1] Migmatitic rock (so-called "Inishi"-type migmatite) of Sakoda et al. (2006). [2] Banded gneiss of Takehara and Horie (2019). [3] Granitic mylonite of Takehara and Horie (2019). (4) Undeformed granite of Takehara and Horie (2019)

Mineral abbreviations in this paper follow Whitney and Evans (2010).

2 | GEOLOGICAL BACKGROUND

2.1 | Geology of the Hida Belt

The continental crust which forms the Japanese Islands is the product of a protracted active Pacific-type orogen resulting from subduction, oceanward-accretion, and landward-erosion, which began in the early-Paleozoic (e.g., Ernst et al., 2007; Isozaki, 1996; Isozaki et al., 2010; Maruyama, 1997; Maruyama et al., 1997). Most basement components of the Japanese Islands have been considered to have grown along the Cathaysia Block of the South China Craton (i.e., "Greater South China," Isozaki, 2019; Isozaki et al., 2014, 2015, 2017). However, the Hida Belt (Figures 1 and 2) is regarded to have the North China Craton affinity (e.g., Isozaki, 1997; Isozaki et al., 2010).

The Hida Belt of central Japan (Figures 1 and 2) is a continental fragment, which was once a part of a crustal basement of the East Asian continental margin prior to the opening of the Japan Sea in the Miocene (e.g., Hiroi, 1981; Isozaki, 1996, 1997; Maruyama et al., 1997; Wakita, 2013). It consists mainly of Permo-Triassic granite-gneiss complexes with impure marble, calc-silicate rock, amphibolite, migmatite, granitic gneiss and minor high-aluminous pelitic schist (cf., Ehiro et al., 2016). These gneissose and granitic rocks are unconformably covered by the Cretaceous Tetori Group sediments with some clasts derived from the basement (e.g., Sano & Yabe, 2017; Tsujimori, 1995). The timing of the amphibolite- to granulite-facies regional metamorphism and related igneous activity has been dated as ∼260–230 Ma (e.g., Horie et al., 2018; Sano et al., 2000; Takahashi et al., 2018). Although the direct depositional age of the protolith of paragneiss is unclear, Late Carboniferous fossils of foraminifera and bryozoa were found in the low-metamorphic grade marble from the Unazuki "sub-belt" of the Hida Belt (Hiroi et al., 1978). The youngest zircon core age of the paragneiss is ∼275 Ma (Takahashi et al., 2018). Based on the cross-cutting and deformational relationships, granitic rocks in the Hida Belt (including their metamorphic equivalents) have been grouped into two types: older mostly deformed syn-metamorphic granitic rocks of ∼250–240 Ma and younger undeformed granitic rocks of ∼200–190 Ma (Kano, 1990a, 1990b; Takahashi et al., 2010; Takehara & Horie, 2019; Zhao et al., 2013). The SHRIMP zircon U–Pb dating of a pyroxene

gneiss from the Amo area has given a Paleoproterozoic concordant detrital age of $\sim$1.84 Ga and Archean upper intercept ages of $\sim$3.42 and $\sim$2.56 Ga (Sano et al., 2000). Detrital zircons from pelitic gneiss of the Tateyama area have a strong age peak at $\sim$1.8 Ga (Takahashi et al., 2018). Such Orosirian zircons are widespread in East Asian continental basements (e.g., Geng, 2015; Kim et al., 2020; Zhao & Zhai, 2013) as well as many continental shields as fragments of the Columbia/Nuna supercontinent (e.g., Ganbat et al., 2021). Moreover, Horie et al. (2010, 2018) reported Eoarchean-Paleoproterozoic inherited zircons in granitic rocks from the Unazuki "sub-belt."

The Kamioka area (Figure 2b) is located on the central part of the Hida Belt. In the area, there is the Pb–Zn ore deposit of the Kamioka Mine (e.g., Kunugiza, 1999; Morishita, 1999; Nakano et al., 1997; Omori & Mariko, 1999) which has been formed at $\sim$60 Ma (Nagasawa & Shibata, 1985; Sato & Uchiumi, 1990). The overall structure of the Kamioka area is characterized by the NS to NE–SW axis fold structure with wavelength of 1–2 km (Kano, 1982; Sohma & Akiyama, 1984). This area consists mainly of granitic and metamorphic rocks such as marble, calc-silicate rock, migmatite and amphibolite. They thrust over the Cretaceous Tetori Group sediments at the northern part of the Kamioka area. The eastern and southern parts of this area are mainly composed of granitic rocks. The carbon isotope geothermometry for coexisting graphite and calcite gives a peak metamorphic temperature of $\sim$600–700 °C (Wada, 1977). The Funatsu Shear Zone, which consists of mylonitic granites and augen gneisses, is located between gneissose and granitic rocks (e.g., Kano, 1973, 1983; Komatsu et al., 1993). The SHRIMP U–Pb zircon dating of the deformed and undeformed granitic rocks suggests that the mylonitization occurred between 240 Ma and 199 Ma (Takahashi et al., 2010; Takehara & Horie, 2019). The younger granitic rocks intruded into the older granitic rocks, and the hornfels-like texture of the older granitic rocks at the boundary suggests a contact metamorphism by the younger granite activity (Kano & Watanabe, 1995).
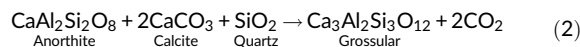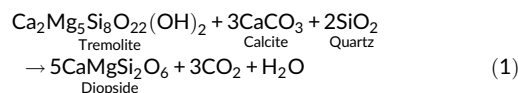
The Wadagawa area (Figure 2a) is located at $\sim$20 km north of the Kamioka area. The metamorphic lithologies of this area consist mainly of marble, calc-silicate rock, amphibolite and migmatite (Suwa et al., 1981). The calc-silicate rock is distributed adjacent to marble. Granitic rocks intruded into gneissose rocks at southern and western parts of this area. In northern part of the Wadagawa area, these gneissose and granitic rocks are unconformably overlain by the Tetori Group sediments. Pelitic gneisses contain the mineral assemblage of sillimanite + K-feldspar and corundum + K-feldspar (Asami, 1979), and the garnet–biotite geothermometry indicates $\sim$700 °C at $\sim$0.4–0.7 GPa (Suzuki et al., 1989).

2.2 | Metacarbonate rocks in the Hida Belt

In the Hida Belt, a large amount of marble occurs accompanying gneissose rocks (Kano, 1998). The protolith of the Hida marble has been regarded to be continental platform carbonates (e.g., Isozaki, 1996, 1997; Sohma & Kunugiza, 1993). Most of the Hida marble consists mainly of calcite (i.e., calcite marble) with a minor

amount of clinopyroxene, quartz, and titanite. Dolomitic marble which consists mainly of Mg-calcite and dolomite is rare; it contains Mg-rich silicates such as forsterite, tremolite, clinohumite, and serpentine (Kano, 1998; Suzuki, 1959). The calcite–dolomite solvus thermometry from the calcite–dolomite intergrowth gives a temperature $\sim$600 °C (Imai et al., 1977; Kano, 1998). Wada and co-authors performed microscale C–O isotope analyses for calcites in marble from the Hida Belt. Microscale C–O isotope zoning was confirmed in calcite crystals near the calcite-calcite and calcite-graphite grain boundaries (Wada, 1988). Arita and Wada (1990) found a sharp decrease of $\delta^{18}O$ values in calcite crystals near grain boundaries (oxygen isotope trough), and they suggested that such an isotope feature had been formed by the isotope exchange with metamorphic fluids which were provided from a granitic pluton. Based on a systematic correlation between $\delta^{18}O$ depletion along calcite-calcite grain boundaries and Mn and Sr concentrations, Graham et al. (1998) estimated a cooling rate after amphibolite-facies conditions.

It is suggested that the tectonic mingling of different types of rocks formed new lithological variations in the Hida Belt (Kunugiza et al., 2010; Kunugiza & Kaneko, 2001). The mingling of marble and orthogneiss formed diopside–hedenbergite series clinopyroxene, and the subsequent infiltration of H_2O-rich fluids, which were mainly derived from granitic rocks, formed grossular garnet. It has generated a carbonate–silicate rock which contains a "skarn-like" mineral assemblage. Diopside and grossular garnet are formed via following reactions.

$$Ca_2Mg_5Si_8O_{22}(OH)_2 + 3CaCO_3 + 2SiO_2$$
$$\underset{\text{Tremolite}}{} \quad \underset{\text{Calcite}}{} \quad \underset{\text{Quartz}}{}$$
$$\rightarrow 5CaMgSi_2O_6 + 3CO_2 + H_2O \qquad (1)$$
$$\underset{\text{Diopside}}{}$$

$$\underset{\text{Anorthite}}{CaAl_2Si_2O_8} + \underset{\text{Calcite}}{2CaCO_3} + \underset{\text{Quartz}}{SiO_2} \rightarrow \underset{\text{Grossular}}{Ca_3Al_2Si_3O_{12}} + 2CO_2 \qquad (2)$$

In the Hida Belt, metallogenic explorations with drill cores were performed by the Metal Mining Agency of Japan (MMAJ) and Ministry of International Trade and Industry (MITI) including C–O isotope compositions of calcites around the Kamioka area, and their isotope compositions show large variations. Although project reports of the MITI and MMAJ (MMAJ, 1995; MITI, 1989, 1992, 1993, 1996, 1997, 1998a, 1998b, 1999, 2000) include many stable isotope data, they lack petrological information corresponding to isotope data and tectonic implications.

3 | SAMPLE DESCRIPTIONS

Investigated samples were selected from eight drill cores which were dug by MITI and MMAJ at the Kamioka area, Gifu Prefecture (Figure 2b); sample selection was based on previous petrological studies by Kunugiza and Kaneko (2001) and Kunugiza et al. (2010). We also investigated one rock sample collected at a surface exposure in the Wadagawa area, Toyama Prefecture (Figure 2a). Based on the

lithological features including mineral assemblage and mineral compositions (see detail in Section 5.1), we grouped the samples into five lithological types (Type 1–5: Table 1).

Type 1–4 samples are marbles from drill cores from the Kamioka area. Type 5 is a carbonate–silicate rock (KK-HD-XAXB) (Figure 3a) collected from an outcrop at a construction site of the check dam in the Wada River, Toyama Prefecture (Figure 2a). Type 5 carbonate–silicate rock is closely associated with diorite, and this type of sample has been described in previous studies (Kunugiza et al., 2010; Kunugiza & Kaneko, 2001).

4 | METHODS

4.1 | Carbon and oxygen stable isotope analysis of calcite

Micro-sampling technique using a hand-held needle drill was applied to analyze C–O stable isotopes. We used a hand-held drill with a clean diamond-tipped drill-bit (0.4 or 1.0 mm in diameter) to mill the target spots under a binocular microscope. To avoid contamination, each target was sampled after mechanical abrasion of surface. We also conducted X-ray diffraction analyses, using a Phillips X'pert-MPD PW3050 XRD at Tohoku University, for sample powders (101 samples). The XRD analyses confirmed the absence of dolomite peaks on their X-ray diffractometer patterns. Thus, we regarded that analyzed all carbonates are calcite. Recovered sample powders ($\sim$0.1 mg) were reacted with 100 % phosphoric acid at $\sim$72 °C, and the isotope compositions were measured with a Thermo Fisher Delta V isotope ratio mass spectrometer equipped with a ThermoQuest Kiel-III automated carbonate device, at Tohoku University. Although some samples contain silicate minerals, they are almost insoluble in 72 °C phosphoric acid. Therefore, the effect of silicate minerals for isotope compositions is negligible. The isotope ratios were expressed in conventional (δ ‰) notation and calibrated to the NBS-19 international standard, relative to Vienna Pee Dee Belemnite (VPDB). The external precisions (1σ) for the carbon and oxygen isotope analyses based on replicate measurements (n = 47) of the laboratory reference materials JCp-1 were 0.03 and 0.04 ‰, respectively. $\delta^{18}O$ [‰ VPDB] is converted to $\delta^{18}O$ [‰ VSMOW] by using the Coplen et al.'s (1983) equation.

4.2 | Sr isotope analysis of calcite

Samples were cut into several millimeters chips and surface was polished. Then, washed rock chips were crushed using an alumina mortar. Prepared samples were dissolved in 2 N HCl at room temperature overnight. Strontium dissolved in the solution was separated chromatographically using cation exchange resin (Bio-Rad AG 50W-X12; 200–400 mesh). Separated Sr was loaded onto degassed single W filaments along with Ta activator, and the Sr isotopes were measured using a thermal ionization mass spectrometer (TIMS: Finnigan MAT-262) at Okayama University. The $^{87}Sr/^{86}Sr$ measurements were

TABLE 1 Summary of petrological characteristics of five lithological types of samples

| Type	Core name	Depth (m)	Locality	Lithology	Mineral assemblage	Silicates (vol%)	Remark
Type 1	45EANG-1	627, 631, 647	Nagato	Pure marble	Cal, ±Cpx, ±Amp	<1	Adjacent to calc-silicate rocks
	1MAHAU-6	90.7	Atotsu	Pure marble	Cal, ±Cpx, ±Ttn	<1	Adjacent to calc-silicate rocks
Type 2	1MAHI-1	575	Inishi	Impure marble	Cal, Afs, Cpx, Qz, ±Pl, ±Grs, ±Wo, ±Ep, ±Ttn, ±Zrn	~20–25	
	1MAHI-1	584.6	Inishi	Impure marble	Cal, Afs, Cpx, ±Qz, ±Pl, ±Ep, ±Ttn, ±Scp, ±Gr	~10	
Type 3	1MAHI-1	582	Inishi	Pure marble	Cal, ±Cpx	<1	Adjacent to quartzo-feldspathic rock
Type 4	57HA-2	501.5	Atotsu	Impure marble	Cal, Qz, Cpx, ±Amp, ±Ep, ±Grs ±Ttn, ±Gr	~5–10	
Type 5	Surface exposure	—	Wadagawa	Carbonate–silicate rock	Cpx, Grs, Cal, Prh, Pl, ±Ep, ±Qz, ±Ttn	~85–90	

Note: See details in text.
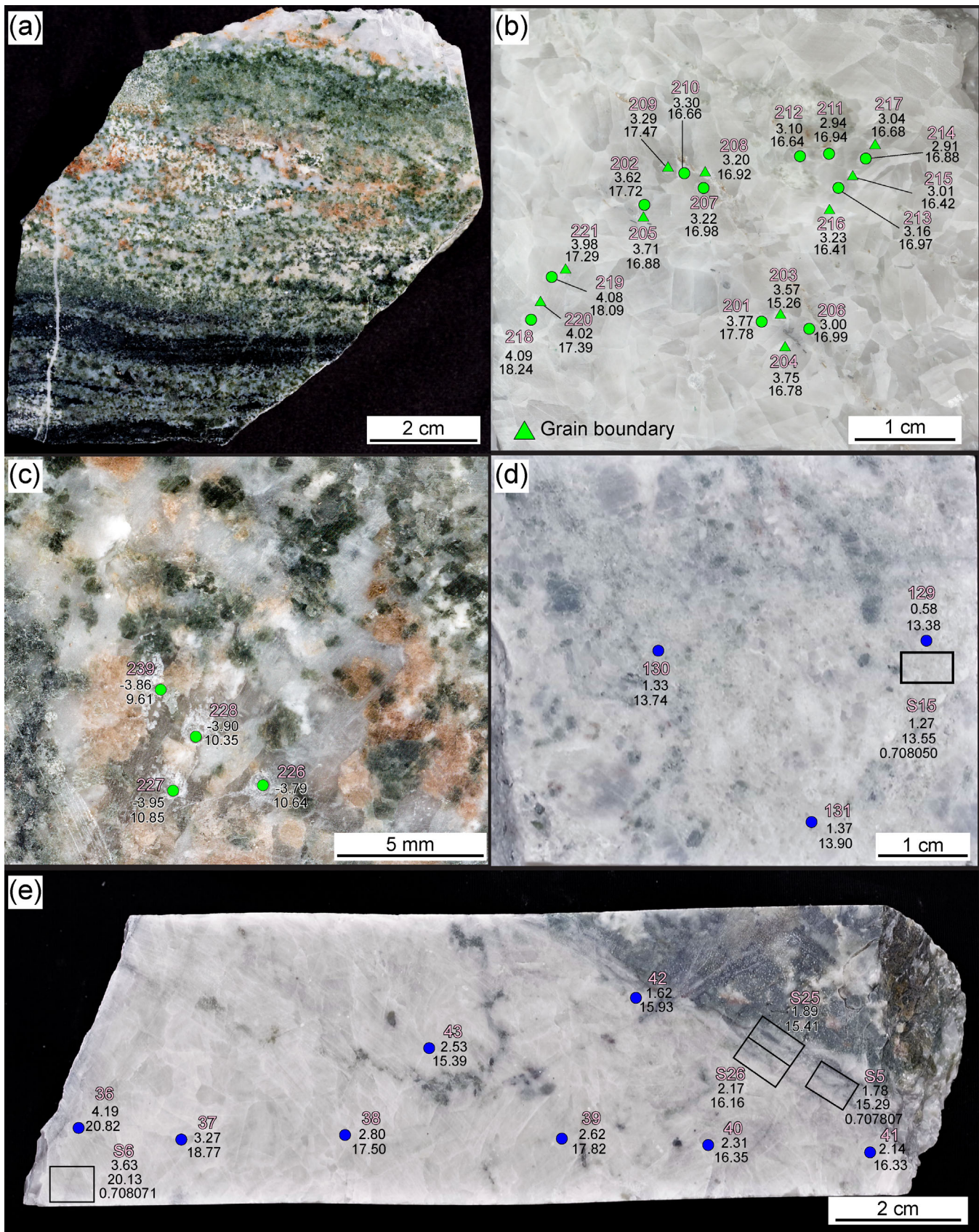
FIGURE 3 (a) Photograph of Type 5 carbonate–silicate rock. (b) C–O isotope analyses spot and isotope compositions of 1MAHI-1-584.6M sampled by a 0.4 mm diameter drill. Upper values are δ^{13}C [‰ VPDB], and lower values are δ^{18}O [‰ VSMOW]. (c) C–O isotope analyses spot and isotope compositions of KK-HD-XAXB sampled by a 0.4 mm diameter drill. (d) C–O isotope analyses spot and isotope compositions of 1MAHI-1-575M sampled by a 1 mm diameter drill. (e) C–O isotope analyses spot and isotope compositions of 45EANG-1-627M sampled by a 1 mm diameter drill
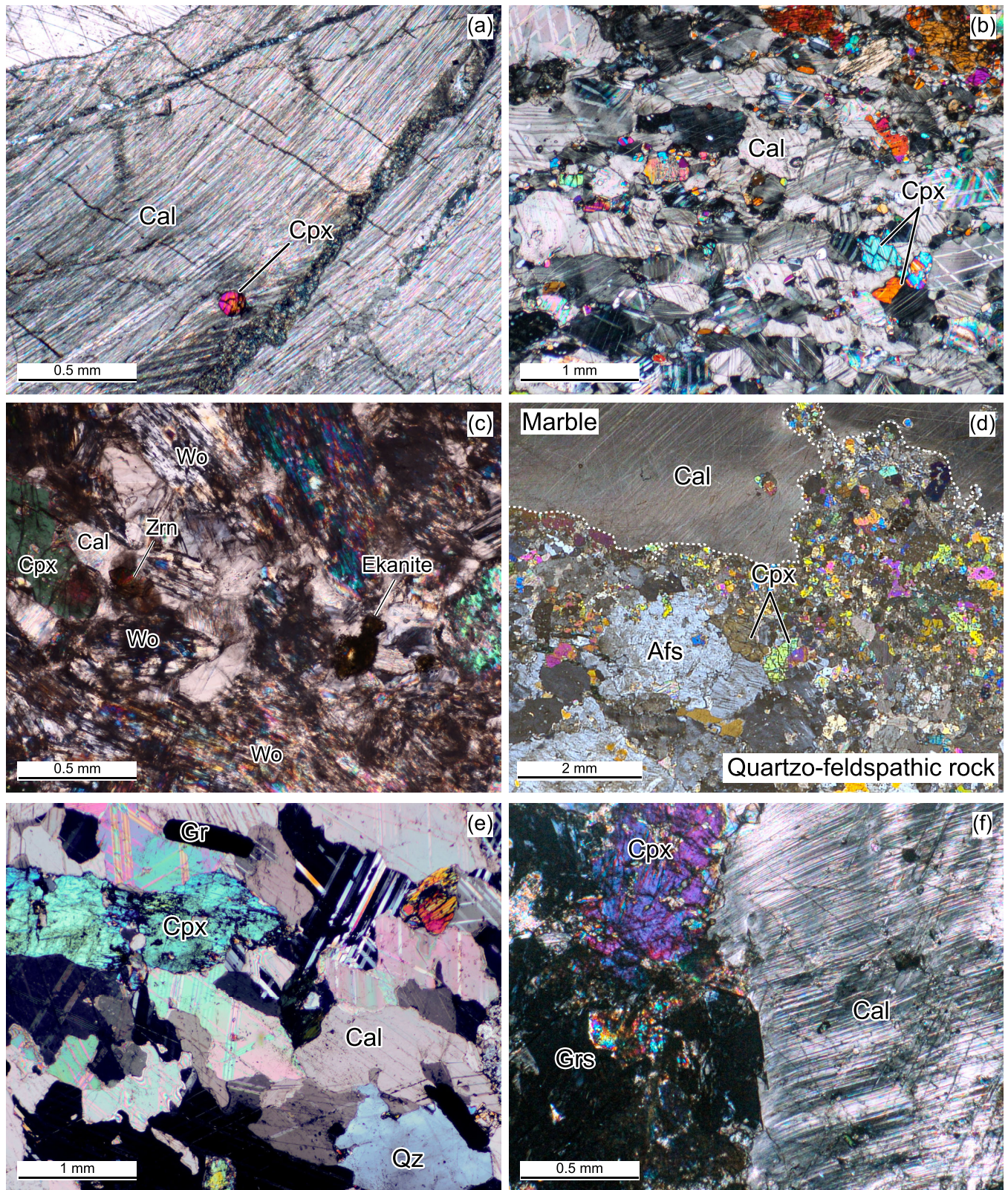
FIGURE 4 (a) Crossed–polarized light (XPL) image of silicates-poor Type 1 marble (45EANG-1-647M). (b) XPL image of silicates-rich Type 2 marble (1MAHI-1-575M). (c) XPL image of wollastonite-rich part of Type 2 marble. Zircon and ekanite occur in this part. (d) XPL image of Type 3 marble with quartzo-feldspathic rock (1MAHI-1-582.0M). (e) XPL image of Type 4 marble (57HA-2-501.5M). (f) XPL image of Type 5 carbonate–silicate rock (KK-HD-XAXB)

normalized to the $^{88}Sr/^{86}Sr$ ratio of 8.375209. The $^{87}Sr/^{86}Sr$ ratio of the NIST987 during the course of this study was 0.710231 ± 0.000027 (2σ). The blank levels were 37 pg and were considered negligible for the Sr isotope analysis.

4.3 | Zircon U–Pb dating

In situ zircon U–Pb dating was carried out in Okayama University of Science by using a Thermo Fisher Scientific iCAP-RQ single-collector quadrupole ICPMS coupled to a Teledyne Cetac Technologies Analyte G2 ArF excimer laser ablation (LA) system equipped with a HelEx 2 volume sample chamber. The LA of zircon was conducted at the condition of laser spot size of 25 μm with fluence of 1.8 J/cm^2 and repetition rate of 5 Hz. Other conditions of LA-ICPMS method are referred to Aoki et al. (2019, 2020).

5 | RESULTS

5.1 | Petrography

Petrological features of each lithological group are described below. All investigated samples show no remarkable foliations and commonly show granoblastic texture. Representative electron microprobe (WDS and EDS: wavelength- and energy-dispersive X-ray spectroscopy) analyses results of clinopyroxenes are shown in Table S1.

5.1.1 | Type 1 marble

Marbles from 45EANG-1-627M, 45EANG-1-631M, and 45EANG-1-647M are composed mainly of coarse-grained calcite (up to ∼5 mm in size) (Figure 4a). Subhedral clinopyroxene (Mg# [= Mg/(Mg + Fe^{2+})] = 0.64–0.92), Ca-amphibole, quartz, apatite, and secondary prehnite occur as accessory minerals. 1MAHAU-6-90.7M is a grayish marble consisting mainly of coarse-grained calcite (up to ∼5 mm in size) with a small amount of clinopyroxene and titanite. Euhedral titanites (up to ∼1 mm, mostly ∼0.2–0.3 mm in length) occur at the boundary with an adjacent calc-silicate rock. Ca-amphibole, apatite and graphite are observed as accessory minerals.

5.1.2 | Type 2 marble

1MAHI-1-575M is a silicate-rich, heterogenous, impure marble that consists mainly of calcite, K-feldspar, clinopyroxene (Mg# = 0.55–0.76) and quartz, with a small amount of plagioclase, grossular garnet (grs$_{94-99}$), wollastonite, epidote, titanite, and secondary prehnite (Figure 4b). Apatite, graphite and a very minor amount of zircon, ekanite, galena, and sphalerite are observed as accessory minerals. Most of calcite grains are ∼0.5 mm and ∼2–3 mm in size. Subhedral clinopyroxene crystals occur with a wide range in size (up to

∼2.5 mm) and sometimes as porphyroblast containing calcite inclusions. Grossular garnet occurs commonly at the boundary between plagioclase and calcite. Wollastonites occur locally and are associated with calcite and quartz (Figures 4c and 6a). Zircon and ekanite occur in the wollastonite-rich part (Figure 4c). Titanites also occur together with wollastonites. 1MAHI-1-584.6M is an impure marble that consists mainly of calcite, K-feldspar and clinopyroxene (Mg# = 0.68–0.94) with a small amount of quartz, plagioclase, epidote, titanite, and secondary prehnite. Apatite, scapolite, allanite, and graphite are observed as accessory minerals. Calcite occurs mainly as coarse-grained crystals (∼2–5 mm in size). K-feldspar occurs as coarse-grained crystals (∼2–5 mm in size) and often contains calcite, quartz, clinopyroxene, and epidote as its inclusions. Clinopyroxene occurs as coarse-grained subhedral crystals (∼1–3 mm in size) and contains calcite inclusions. It rarely occurs as fine-grained crystals (∼0.2–0.3 mm in size) and forms equigranular texture with quartz and calcite.

5.1.3 | Type 3 marble

1MAHI-1-582.0M is a marble adjacent to quartzo-feldspathic rock (Figure 4d). The marble part consists mainly of calcite with a small amount of clinopyroxene. In contrast, quartzo-feldspathic rock consists mainly of quartz, K-feldspar and plagioclase with a small amount of calcite, clinopyroxene (Mg# = 0.47–0.57), Ca-amphibole, epidote, and secondary chlorite. Titanite, apatite, and allanite are observed as accessory minerals. K-feldspar occurs as coarse-grained crystals (up to ∼5 mm in size) and contains quartz and calcite inclusions. Subhedral clinopyroxene crystals occur mainly near the boundary of quartzo-feldspathic rock and marble. Calcite, quartz, and clinopyroxene show an equigranular texture (∼0.5 mm in size) near the boundary of marble and quartzo-feldspathic rock.

5.1.4 | Type 4 marble

57HA-2-501.5M is an impure marble, and it consists mainly of calcite, quartz, and clinopyroxene, with a small amount of Ca-amphibole (tremolite–actinolite), epidote, grossular garnet (grs$_{90}$), titanite, and graphite (Figure 4e). Apatite, chlorite, and allanite are observed as accessory minerals. Calcite occurs as anhedral crystals with a wide range in size (∼0.1–4 mm in size). Subhedral clinopyroxene shows dusty appearance with a wide range in size (up to ∼0.6 mm in size). It often grows on Ca-amphibole and shows a wide range of Mg# (0.38–0.93). Clinopyroxene has relatively heterogeneous compositions. In general, Fe-rich clinopyroxenes occur at secondary cracks and have high MnO content, containing up to 3.3 wt%. Graphite occurs as elongate-shaped crystals and reaches up to ∼2 mm in length.

5.1.5 | Type 5 carbonate–silicate rock

Type 5 carbonate–silicate rock consists mainly of clinopyroxene (Mg# = 0.43–0.54), grossular garnet (grs$_{84-93}$), calcite, prehnite, and

TABLE 2 Carbon ($\delta^{13}C$) and oxygen ($\delta^{18}O$) isotope compositions of calcite

Analysis ID	Sample name	$\delta^{13}C$ [‰ VPDB]	$\delta^{18}O$ [‰ VSMOW]
#0	45EANG-1-647M	+3.72	+13.82
#1	45EANG-1-647M	+3.67	+14.97
#2	45EANG-1-647M	+3.36	+ 11.19
#3	45EANG-1-647M	+3.63	+12.33
#4	45EANG-1-647M	+3.33	+8.69
#5	45EANG-1-647M	+3.41	+9.74
#6	45EANG-1-647M	+3.88	+12.97
#7	45EANG-1-647M	+3.88	+13.47
#8	45EANG-1-647M	+3.68	+13.55
#9	45EANG-1-647M	+3.42	+13.96
#10	45EANG-1-647M	+3.66	+14.03
#11	45EANG-1-647M	+3.48	+13.42
#12	45EANG-1-647M	+3.75	+13.68
#13	45EANG-1-647M	+3.05	+12.94
#14	45EANG-1-647M	+3.41	+13.87
#15	45EANG-1-647M	+3.91	+13.82
#16	45EANG-1-647M	+3.39	+14.24
#17	45EANG-1-647M	+3.77	+14.28
#18	45EANG-1-647M	+3.68	+14.60
#19	45EANG-1-647M	+3.73	+11.86
#20	45EANG-1-647M	+3.66	+12.54
#21	45EANG-1-647M	+3.47	+13.56
#22	45EANG-1-647M	+3.62	+ 14.19
#23	45EANG-1-647M	+3.13	+13.46
#24	45EANG-1-627M	+3.54	+18.40
#25	45EANG-1-627M	+3.47	+18.21
#26	45EANG-1-627M	+3.54	+ 18.16
#27	45EANG-1-627M	+3.55	+ 19.13
#28	45EANG-1-627M	+3.55	+20.25
#29	45EANG-1-627M	+3.47	+17.33
#30	45EANG-1-627M	+3.61	+18.95
#31	45EANG-1-627M	+2.87	+14.77
#32	45EANG-1-627M	+3.62	+19.37
#33	45EANG-1-627M	+3.56	+18.02
#34	45EANG-1-627M	+3.66	+16.90
#35	45EANG-1-627M	+3.29	+18.07
#36	45EANG-1-627M	+4.19	+20.82
#37	45EANG-1-627M	+3.27	+18.77
#38	45EANG-1-627M	+2.80	+17.50
#39	45EANG-1-627M	+2.62	+17.82
#40	45EANG-1-627M	+2.31	+16.35
#41	45EANG-1-627M	+2.14	+16.33
#42	45EANG-1-627M	+1.62	+15.93
#43	45EANG-1-627M	+2.53	+15.39
#44	45EANG-1-631M	+2.78	+14.38
#45	45EANG-1-631M	+2.80	+14.23

(Continues)

TABLE 2 (Continued)

Analysis ID	Sample name	δ¹³C [‰ VPDB]	δ¹⁸O [‰ VSMOW]
#46	45EANG-1-631M	+2.85	+14.04
#47	45EANG-1-631M	+2.38	+13.30
#48	45EANG-1-631M	+2.38	+13.37
#49	45EANG-1-631M	+2.68	+13.68
#50	45EANG-1-631M	+2.70	+14.48
#51	45EANG-1-631M	+2.28	+14.30
#52	1MAHI-1-582.0M	−0.25	+ 14.10
#53	1MAHI-1-584.6M	+2.97	+14.65
#54	1MAHI-1-584.6M	+3.07	+14.58
#55	1MAHI-1-584.6M	+2.95	+14.94
#56	1MAHI-1-584.6M	+3.05	+15.04
#57	1MAHI-1-584.6M	+1.56	+ 15.16
#58	1MAHI-1-584.6M	+2.14	+16.35
#59	1MAHI-1-584.6M	+2.69	+14.76
#60	1MAHI-1-584.6M	+3.20	+16.79
#61	1MAHI-1-584.6M	+4.00	+17.59
#62	1MAHI-1-584.6M	+4.04	+18.39
#63	1MAHI-1-584.6M	+3.83	+18.09
#64	1MAHI-1-584.6M	+3.81	+18.76
#65	1MAHI-1-584.6M	+0.45	+18.83
#66	1MAHI-1-584.6M	+3.49	+18.30
#67	1MAHAU-6-90.7M	+2.62	+13.08
#68	1MAHAU-6-90.7M	+3.23	+14.58
#69	1MAHAU-6-90.7M	+3.17	+14.00
#70	1MAHAU-6-90.7M	+2.27	+12.31
#71	1MAHAU-6-90.7M	+3.17	+13.99
#72	1MAHAU-6-90.7M	+3.24	+14.41
#73	1MAHAU-6-90.7M	+3.02	+14.38
#74	1MAHAU-6-90.7M	+3.21	+14.39
#75	1MAHAU-6-90.7M	+3.47	+14.27
#76	1MAHAU-6-90.7M	+3.43	+14.51
#77	1MAHAU-6-90.7M	+3.07	+14.17
#78	1MAHAU-6-90.7M	+3.93	+14.06
#79	1MAHAU-6-90.7M	+3.68	+14.20
#80	1MAHAU-6-90.7M	+3.51	+14.21
#81	1MAHAU-6-90.7M	+3.75	+14.18
#82	1MAHAU-6-90.7M	+3.56	+14.46
#83	1MAHAU-6-90.7M	+3.74	+14.27
#84	1MAHAU-6-90.7M	+3.77	+14.08
#85	1MAHAU-6-90.7M	+3.86	+13.68
#86	1MAHAU-6-90.7M	+3.30	+13.81
#87	1MAHAU-6-90.7M	+2.53	+14.03
#88	1MAHAU-6-90.7M	+3.57	+13.81
#89	1MAHAU-6-90.7M	+3.42	+13.90
#90	1MAHAU-6-90.7M	+3.68	+13.58
#91	1MAHAU-6-90.7M	+3.14	+13.31

TABLE 2 (Continued)

Analysis ID	Sample name	δ¹³C [‰ VPDB]	δ¹⁸O [‰ VSMOW]
#92	1MAHAU-6-90.7M	+3.19	+13.59
#93	1MAHAU-6-90.7M	+2.24	+13.22
#94	1MAHAU-6-90.7M	+3.78	+13.85
#95	1MAHAU-6-90.7M	+3.73	+14.02
#96	1MAHAU-6-90.7M	+3.53	+13.50
#97	1MAHAU-6-90.7M	+3.01	+13.40
#98	1MAHAU-6-90.7M	+3.15	+13.25
#99	1MAHAU-6-90.7M	+3.93	+13.17
#100	1MAHAU-6-90.7M	+3.63	+13.85
#101	1MAHAU-6-90.7M	+3.38	+13.86
#102	1MAHAU-6-90.7M	+3.87	+13.95
#103	57HA-2-501.5M	+3.07	+7.03
#104	57HA-2-501.5M	+3.28	+8.19
#105	57HA-2-501.5M	+3.07	+5.00
#106	57HA-2-501.5M	+2.95	+8.91
#107	57HA-2-501.5M	+2.64	+5.88
#108	57HA-2-501.5M	+2.42	+5.27
#109	57HA-2-501.5M	+3.90	+9.63
#110	57HA-2-501.5M	+2.98	+9.24
#111	57HA-2-501.5M	+2.61	+4.52
#112	57HA-2-501.5M	+2.43	+8.96
#113	57HA-2-501.5M	+2.60	+3.27
#114	57HA-2-501.5M	+2.11	+5.06
#115	57HA-2-501.5M	+2.02	+3.53
#116	57HA-2-501.5M	+1.58	+4.52
#117	57HA-2-501.5M	+1.33	+3.84
#118	57HA-2-501.5M	+2.13	+8.00
#123	1MAHI-1-575M	−0.10	+14.08
#124	1MAHI-1-575M	−0.02	+13.23
#125	1MAHI-1-575M	+1.37	+13.16
#126	1MAHI-1-575M	+1.56	+13.68
#127	1MAHI-1-575M	+1.97	+13.48
#128	1MAHI-1-575M	+1.21	+13.63
#129	1MAHI-1-575M	+0.58	+13.38
#130	1MAHI-1-575M	+1.33	+13.74
#131	1MAHI-1-575M	+1.37	+13.90
#132	1MAHI-1-575M	+0.25	+13.21
#133	1MAHI-1-584.6M	+0.20	+15.26
#134	1MAHI-1-584.6M	+1.33	+15.11
#135	1MAHI-1-584.6M	+3.99	+17.37
#136	1MAHI-1-584.6M	+2.06	+15.99
#137	1MAHI-1-584.6M	+2.87	+16.93
#138	1MAHI-1-584.6M	+3.56	+17.07
#139	1MAHI-1-582.0M	+0.82	+14.31
#140	1MAHI-1-582.0M	+1.11	+14.15
#141	45EANG-1-647M	+3.41	+13.64

(Continues)

TABLE 2   (Continued)

Analysis ID	Sample name	δ^{13}C [‰ VPDB]	δ^{18}O [‰ VSMOW]
#2-1	KK-HD-XAXB	−4.30	+11.06
#2-2	KK-HD-XAXB	−4.42	+11.41
#2-3	KK-HD-XAXB	−4.02	+10.52
#2-4	KK-HD-XAXB	−4.09	+10.57
#S1	KK-HD-XAXB	−2.93	+9.65
#S2	KK-HD-XAXB	−4.30	+10.52
#S3	KK-HD-XAXB	−4.10	+10.31
#S4	45EANG-1-627M	+3.53	+18.46
#S5	45EANG-1-627M	+1.78	+15.29
#S6	45EANG-1-627M	+3.63	+20.13
#S7	45EANG-1-631M	+2.70	+ 13.19
#S8	45EANG-1-647M	+3.51	+13.67
#S9	45EANG-1-647M	+3.79	+12.62
#S10	57HA-2-501.5M	+2.82	+6.10
#S11	57HA-2-501.5M	+3.82	+10.44
#S12	57HA-2-501.5M	+1.47	+3.94
#S13	1MAHI-1-575M	+1.57	+13.63
#S14	1MAHI-1-575M	+0.17	+13.22
#S15	1MAHI-1-575M	+1.27	+13.55
#S16	1MAHI-1-582.0M	−0.01	+13.95
#S17	1MAHI-1-584.6M	+3.12	+14.43
#S18	1MAHI-1-584.6M	+0.02	+15.48
#S19	1MAHI-1-584.6M	+3.99	+17.60
#S20	1MAHAU-6-90.7M	+3.60	+14.09
#S21	1MAHAU-6-90.7M	+3.37	+ 13.15
#S22	1MAHAU-6-90.7M	+3.79	+13.48
#S23	1MAHAU-6-90.7M	+3.62	+13.47
#S24	1MAHAU-6-90.7M	+3.64	+13.54
#S25	45EANG-1-627M	+1.89	+15.41
#S26	45EANG-1-627M	+2.17	+ 16.16
#S27	1MAHI-1-584.6M	+3.18	+18.36
#S28	1MAHAU-6-90.7M	+3.98	+13.78
#201	1MAHI-1-584.6M	+3.77	+17.78
#202	1MAHI-1-584.6M	+3.62	+17.72
#203	1MAHI-1-584.6M	+3.57	+15.26
#204	1MAHI-1-584.6M	+3.75	+16.78
#205	1MAHI-1-584.6M	+3.71	+16.88
#206	1MAHI-1-584.6M	+3.00	+16.99
#207	1MAHI-1-584.6M	+3.22	+16.98
#208	1MAHI-1-584.6M	+3.20	+16.92
#209	1MAHI-1-584.6M	+3.29	+17.47
#210	1MAHI-1-584.6M	+3.30	+16.66
#211	1MAHI-1-584.6M	+2.94	+16.94
#212	1MAHI-1-584.6M	+3.10	+16.64
#213	1MAHI-1-584.6M	+3.16	+16.97
#214	1MAHI-1-584.6M	+2.91	+16.88

TABLE 2 (Continued)

Analysis ID	Sample name	$\delta^{13}C$ [‰ VPDB]	$\delta^{18}O$ [‰ VSMOW]
#215	1MAHI-1-584.6M	+3.01	+16.42
#216	1MAHI-1-584.6M	+3.23	+16.41
#217	1MAHI-1-584.6M	+3.04	+16.68
#218	1MAHI-1-584.6M	+4.09	+18.24
#219	1MAHI-1-584.6M	+4.08	+18.09
#220	1MAHI-1-584.6M	+4.02	+17.39
#221	1MAHI-1-584.6M	+3.98	+17.29
#222	1MAHI-1-584.6M	+0.34	+15.90
#223	1MAHI-1-584.6M	+0.40	+15.63
#224	1MAHI-1-584.6M	+0.38	+15.64
#225	1MAHI-1-584.6M	+0.14	+16.04
#226	KK-HD-XAXB	−3.79	+10.64
#227	KK-HD-XAXB	−3.95	+10.85
#228	KK-HD-XAXB	−3.90	+10.35
#229	1MAHI-1-582.0M	+0.07	+13.82
#230	1MAHI-1-582.0M	−0.55	+13.79
#231	1MAHI-1-582.0M	+0.25	+14.23
#232	57HA-2-501.5M	+2.94	+13.06
#233	57HA-2-501.5M	+2.67	+4.65
#234	57HA-2-501.5M	+1.60	+4.48
#235	57HA-2-501.5M	+1.22	+1.58
#236	57HA-2-501.5M	+0.71	+3.69
#237	57HA-2-501.5M	+3.24	+4.47
#238	57HA-2-501.5M	+3.70	+13.94
#239	KK-HD-XAXB	−3.86	+9.61

Note: Data #0–#141 and data #2-1–#2-4 were sampled by 1 mm diameter drill, data #S1–#S28 were crushed using an alumina mortar, data #201–#239 were sampled by 0.4 mm diameter drill.

plagioclase with a small amount of epidote, quartz, and titanite (Figure 4f). Allanite, apatite and a very minor amount of iron-sulfide, sphalerite, and chalcopyrite are observed as accessory minerals. Clinopyroxene occurs as coarse-grained crystals (up to ∼1.5 mm in size) and contains calcite and quartz inclusions. Grossular garnet has irregular morphology and often forms surrounding clinopyroxene. It contains clinopyroxene, calcite, plagioclase, epidote, and titanite as inclusions. These "skarn-like" mineral assemblages and lithologies (Figure 3a,b) suggest that Type 5 carbonate–silicate rock is a reaction product between marble and orthogneiss.

5.2 | Carbon and oxygen isotope compositions

Total 209 C–O isotope analyses of calcites from 9 samples were performed in this study (Table 2 and Figure 5). Analyses spots are shown in Figures S1–S13. Analyzed data show a wide range of $\delta^{13}C$ [VPDB] and $\delta^{18}O$ [VSMOW] values (from −4.42 to +4.19 ‰ and +1.58 to

+20.82 ‰, respectively; Figure 5) as the same as the previous studies. Isotope trends of each lithological group are described below.

5.2.1 | Type 1 marble

Type 1 marble (n = 103) has relatively constant and high $\delta^{13}C$ values: they are from +1.62 to +4.19 ‰, and 92 out of 103 spots show $\delta^{13}C$ > +2.5 ‰. On the other hand, $\delta^{18}O$ values show a large variation (from +8.69 to +20.82 ‰).

45EANG-1-627M (n = 25) has $\delta^{13}C$ values from +1.62 to +4.19 ‰ and $\delta^{18}O$ values from +14.77 to +20.82 ‰. Micro-sampling (ms) #36 has the highest $\delta^{13}C$ and $\delta^{18}O$ values of this study (+4.19 and +20.82 ‰, respectively). Low $\delta^{13}C$ values (<+2.5 ‰) are obtained near the contact of greenish calc-silicate rock (<∼2 cm from the contact) (Figure 3e). 45EANG-1-631M (n = 9) shows relatively constant $\delta^{13}C$ and $\delta^{18}O$ values (from +2.28 to +2.85 ‰ and +13.18 to +14.48 ‰, respectively). 45EANG-1-647M (n = 27) has relatively constant $\delta^{13}C$ values (from +3.05 to +3.91 ‰) with a wide range of $\delta^{18}O$
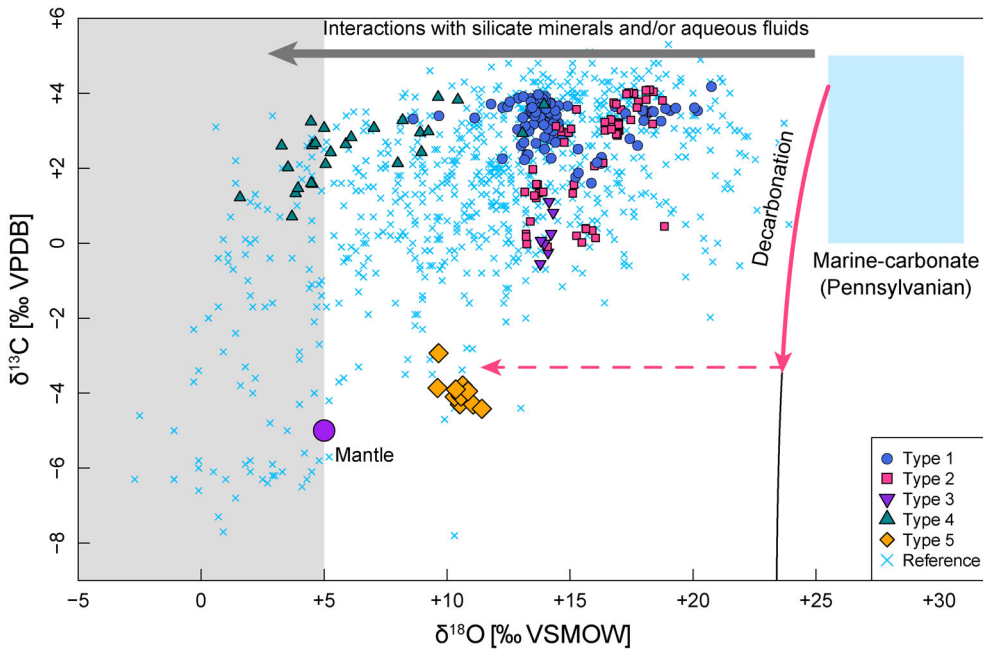
FIGURE 5 C–O isotope variations of marble from the Hida Belt. Data include this study and previous studies (MMAJ, 1995; MITI, 1989, 1992, 1993, 1996, 1997, 1998a, 1998b, 1999, 2000; Wada, 1977). Marine-carbonate area shows late Carboniferous (Pennsylvanian) carbonate $\delta^{13}C$ (Saltzman & Thomas, 2012) and brachiopod $\delta^{18}O$ values (Grossman, 2012). The curve shows the Rayleigh decarbonation effects for C–O isotope compositions of calcite in the Hida marble, using Chacko et al.'s (1991) fractionation factor at T = 700 °C. The initial isotope compositions are assumed as $\delta^{13}C$ = +4.19 ‰ (highest $\delta^{13}C$ values of this study: ms#36) and $\delta^{18}O$ = +25 ‰. Interactions of marble with silicate minerals and/or aqueous fluids would cause $\delta^{18}O$ shift. The $\delta^{18}O$ values lower than mantle value (∼+5 ‰) imply an involvement of meteoric water

values (from +8.69 to +14.97 ‰). 1MAHAU-6-90.7M (n = 42) shows $\delta^{13}C$ values from +2.24 to +3.98 ‰ and $\delta^{18}O$ values from +12.31 to +14.58 ‰. Any $\delta^{13}C$–$\delta^{18}O$ shift was not observed near the contact part with greenish calc-silicate rocks from 45EANG-1-631M, 45EANG-1-647M, and 1MAHAU-6-90.7M.

5.2.2 | Type 2 marble

Type 2 marble (n = 62) shows a moderate variation of $\delta^{13}C$ values (from −0.10 to +4.09 ‰) with a small variation of $\delta^{18}O$ values (from +13.16 to +18.83 ‰).

  1MAHAI-1-575M (n = 13) has nearly constant $\delta^{13}C$ (from −0.10 to +1.97 ‰) and $\delta^{18}O$ values (from +13.16 to +14.08 ‰). Its $\delta^{13}C$ values are relatively low, and two micro-sampling spots (ms#123, #124) show negative $\delta^{13}C$ values (−0.10 and −0.02 ‰, respectively). 1MAHAI-1-584.6M (n = 49) shows $\delta^{13}C$ values from +0.02 to +4.09 ‰ and $\delta^{18}O$ values from +14.42 to +18.83 ‰. The samplings of the ms# 201–225 were performed at grain cores and grain boundaries using a 0.4 mm diameter drill. The core and the grain boundary of calcite crystals have similar $\delta^{13}C$ values. On the other hand, $\delta^{18}O$ values of grain boundary parts are lower than those of core parts (Figure 3b). Calcite crystals near graphites (ms#201–#206, n = 6) have similar $\delta^{13}C$ and $\delta^{18}O$ values to other sampling spots.

5.2.3 | Type 3 marble

Type 3 marble of 1MAHI-1-582.0M (n = 7) has relatively low $\delta^{13}C$ values around 0 ‰ (from −0.55 to +1.11 ‰) with $\delta^{18}O$ values from +13.79 to +14.31 ‰.

5.2.4 | Type 4 marble

Type 4 marble of 57HA-2-501.5M (n = 26) shows a moderate variation of $\delta^{13}C$ (from +0.71 to +3.90 ‰) and low $\delta^{18}O$ values (from +1.58 to +13.94 ‰). Near the brownish vein (ms#234, #235), low $\delta^{18}O$ values were observed (+4.48 and +1.58 ‰, respectively). Two samples which were sampled ∼2 mm away from each other (ms#232 and #233, #237 and #238) show large $\delta^{18}O$ differences (∼9 ‰).

5.2.5 | Type 5 carbonate–silicate rock

Type 5 carbonate–silicate rock (n = 11) is characterized by low $\delta^{13}C$ values (from −4.42 to −2.93 ‰) and shows a small variation of $\delta^{18}O$ values (from +9.61 to +11.41 ‰). Note that $\delta^{13}C$ values of this sample are similar to the upper mantle value (∼−5 ‰). The ms#226, #227, #228, and #239 were sampled from an area of 5 × 5 mm
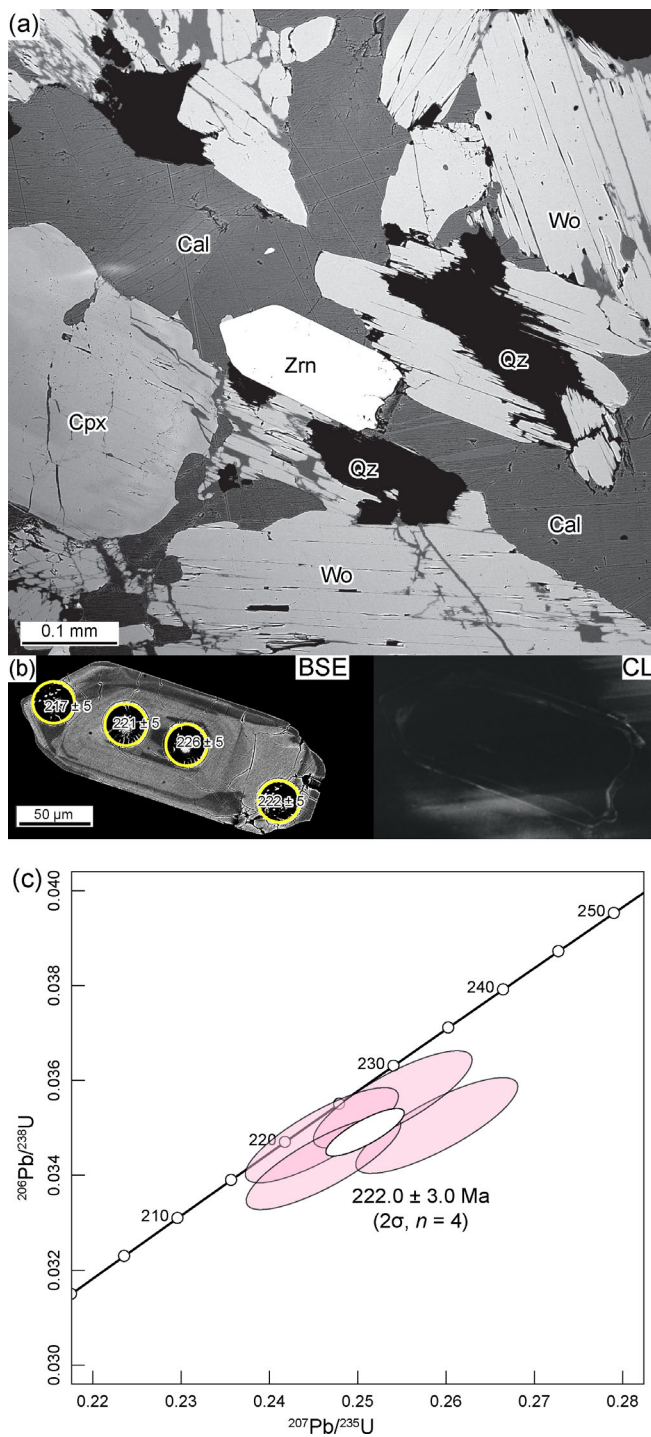
FIGURE 6 (a) Back-scattered electron (BSE) image including the analyzed zircon grain. The zircon is closely associated with wollastonite, calcite and quartz. (b) BSE (left) and cathodoluminescence (CL; right) images of the analyzed zircon grain with analyzed spots. Note that the CL was weak and unclear. (c) The concordia diagram showing zircon U–Pb data. Data plotting and age calculation were performed using IsoplotR (Vermeesch, 2018)

5.3 | Sr isotope ratios

Total 24 Sr isotope analyses were performed on calcite from selected samples (Table 3). Overall analyzed calcites show a small variation (0.707255–0.708220) of $^{87}Sr/^{86}Sr$ ratios, and there is no correlation between C–O isotope data and $^{87}Sr/^{86}Sr$ ratios.

5.4 | Zircon U–Pb age

LA-ICPMS in situ U–Pb dating was performed for a euhedral zircon (~200 μm in length) on a thin-section of 1MAHI-1-575M (Figures 4c and 6). The zircon is closely associated with wollastonite, calcite, and quartz (Figure 6a). Although the zircon shows zonal texture on a BSE image, a cathodoluminescence (CL) image of the zircon is unclear (Figure 6b). The results of zircon U–Pb data are presented in Table 4 and are plotted on the concordia diagram (Figure 6c). The concordance is defined as values of 100 % × ($^{206}Pb/^{238}U$ age)/($^{207}Pb/^{235}U$ age), and analyzed spots have 94.9–98.9 % concordance. Hence, we consider that obtained U–Pb isotope data are concordant. The $^{206}Pb/^{238}U$ ages show 226–217 Ma, and the zircon shows low Th/U ratios (0.04–0.09). The concordia age is 222.0 ± 3.0 Ma (2σ, n = 4).

6 | DISCUSSION

6.1 | Age of crystallization

The CL image of the analyzed zircon is unclear, and the zircon does not show a distinct oscillatory structure in the CL image in contrast with a zoning in the BSE image (Figure 6b). It is known that the zoning features of zircon visible on CL image are not always consistent with the features observed in the BSE image (e.g., McAleer et al., 2020). An oscillatory structure in CL image is a common feature of the most magmatic zircons (e.g., Corfu et al., 2003). Therefore, the lack of oscillatory structure prefers a metamorphic origin rather than a detrital magmatic zircon. Significantly low Th/U values (0.04–0.09) also support the metamorphic origin. There is no textural evidence suggesting a dissolution–reprecipitation process (e.g., Corfu et al., 2003). Moreover, there are some wollastonite crystals coexisting with the analyzed zircon grain (Figures 4c and 6a). In general, wollastonite is formed by the reaction of calcite and quartz in calcareous rocks, which is induced by a decrease of CO_2 content in fluid (i.e., decrease of X_{CO_2}) and/or an increase of temperature (e.g., Bucher & Grapes, 2011; Philpotts & Ague, 2009). The occurrence of wollastonite is rare in other parts of this sample and also other samples, and the coexistence of calcite + quartz assemblage and wollastonite (Figure 6a) is observed. These imply that a fluid-involved recrystallization would have formed both zircon and wollastonite. The occurrence of ekanite (U and Th rich silicate mineral) in wollastonite-rich part (Figure 4c) indicates a local enrichment of U and Th via infiltrating fluid. In addition, newly-formed titanites also occur in the wollastonite-rich part, implying that the fluid was enriched in high field strength elements such as Ti and Zr. These

(Figure 3c). Since these isotope compositions are small variations ($\delta^{13}C$ = −3.95 to −3.79 ‰; $\delta^{18}O$ = +9.61 to +10.85 ‰), they have nearly homogeneous $\delta^{13}C$ and $\delta^{18}O$ values within the area.

TABLE 3 Strontium isotope ratios ($^{87}Sr/^{86}Sr$) of analyzed calcite

Analysis ID	Sample name	$^{87}Sr/^{86}Sr$	2σ
#S1	KK-HD-XAXB	0.708209	0.000008
#S2	KK-HD-XAXB	0.707270	0.000010
#S3	KK-HD-XAXB	0.707264	0.000007
#S4	45EANG-1-627M	0.708136	0.000008
#S5	45EANG-1-627M	0.707807	0.000009
#S6	45EANG-1-627M	0.708071	0.000009
#S7	45EANG-1-631M	0.707905	0.000008
#S8	45EANG-1-647M	0.707861	0.000008
#S9	45EANG-1-647M	0.708028	0.000009
#S10	57HA-2-501.5M	0.707704	0.000008
#S11	57HA-2-501.5M	0.707707	0.000008
#S12	57HA-2-501.5M	0.707758	0.000008
#S13	1MAHI-1-575M	0.707751	0.000009
#S14	1MAHI-1-575M	0.707807	0.000007
#S15	1MAHI-1-575M	0.708050	0.000008
#S16	1MAHI-1-582.0M	0.708220	0.000008
#S17	1MAHI-1-584.6M	0.708139	0.000007
#S18	1MAHI-1-584.6M	0.708157	0.000009
#S19	1MAHI-1-584.6M	0.708062	0.000010
#S20	1MAHAU-6-90.7M	0.707299	0.000010
#S21	1MAHAU-6-90.7M	0.707255	0.000008
#S22	1MAHAU-6-90.7M	0.707411	0.000009
#S23	1MAHAU-6-90.7M	0.707305	0.000009
#S24	1MAHAU-6-90.7M	0.707278	0.000009

facts also support the metamorphic origin of the zircon. In this study, we prefer to interpret that the zircon age of 222.0 ± 3.0 Ma represents the timing of the recrystallization of marble, which was triggered by H_2O-rich fluid infiltration at a relatively high-temperature condition. However, the possibility cannot be also ruled out that the zircon was a detrital grain entrapped in the protolith stage, and the zircon age might have been reset during metamorphism (Yui et al., 2013; Yui & Fukuyama, 2015).

Comparing with other geochronological studies in the Hida Belt (Figure 7), our zircon U–Pb age (222.0 ± 3.0 Ma) corresponds to a later stage of the Permo-Triassic regional metamorphism (∼260–230 Ma). A large amount of the "Inishi"-type migmatite occurs around this drill hole (Inishi area: e.g., Nozawa, 1952; Sakoda et al., 2006), and Sakoda et al. (2006) reported the zircon U–Pb age (234.2 ± 1.8 Ma) of the migmatitic rock from the same borehole (1MAHI-1 766.2–766.7 m). Although our zircon U–Pb age is slightly younger than this age, an infiltrating fluid which caused the wollastonite formation might have related to the regional anatectic event in the Hida Belt.

6.2 | C–O isotope variations

The protolith of the Hida marble has been considered to be continental platform carbonate sediments because of the lithological features

TABLE 4 LA-ICPMS U–Pb isotope data of a zircon in a thin-section of an impure marble (1MAHI-1-575M)

Spot ID	$^{207}Pb/^{235}U$	2σ	$^{206}Pb/^{238}U$	2σ	$^{207}Pb/^{206}Pb$	2σ	$^{207}Pb/^{235}U$ age	2σ	$^{206}Pb/^{238}Pb$ age	2σ	$^{207}Pb/^{206}Pb$ age	2σ	U (μg/g)	Th (μg/g)	Th/U
1	0.259	0.008	0.0350	0.0008	0.0536	0.0009	233.9	6.1	222.1	5.1	354.8	38.1	4381	197	0.045
2	0.254	0.007	0.0356	0.0008	0.0518	0.0009	229.9	6.0	225.5	5.2	275.1	38.5	4950	372	0.075
3	0.246	0.007	0.0348	0.0008	0.0512	0.0009	223.4	5.8	220.8	5.1	250.5	38.2	6682	576	0.086
4	0.246	0.007	0.0343	0.0008	0.0521	0.0009	223.5	5.8	217.2	5.0	290.8	38.8	3995	81	0.020

FIGURE 7 Summary of geochronological studies in the Hida Belt. Magmatic*—magmatic zircon ages including inherited cores, detrital grains and unclear interpretation; magmatic**—zircon ages of younger granitic rocks. Geochronological data are from Horie et al. (2013), Horie et al. (2010, 2018), Koizumi and Otoh (2020), Sakoda et al. (2006), Takahashi et al. (2010, 2018), Takehara and Horie (2019), and Zhao et al. (2013)
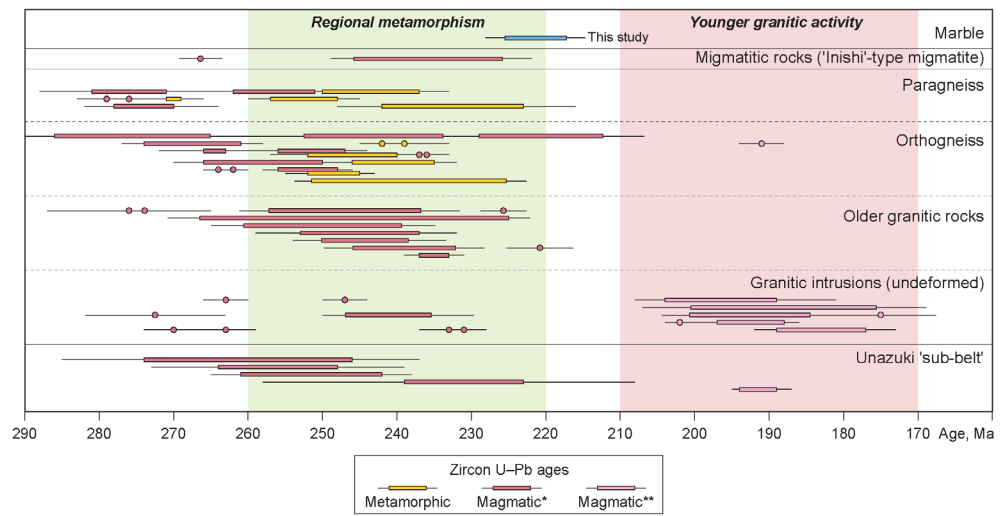
of gneissose rocks and impurity of marbles (e.g., Isozaki, 1996, 1997; Sohma & Kunugiza, 1993). Although the direct depositional age of the protolith of the marble is unclear, based on the occurrence of Late Carboniferous fossils of foraminifera and bryozoa from the Unazuki "sub-belt" of the Hida Belt (Hiroi et al., 1978), we compare our data with Late Carboniferous (Pennsylvanian) carbonate $\delta^{13}C$ (Saltzman & Thomas, 2012) and brachiopod $\delta^{18}O$ (Grossman, 2012) values as a nominal reference of marine-carbonate C–O isotope values.

6.2.1 | Decarbonation reaction effects for $\delta^{13}C$ values

Some samples contain a trace amount of graphite. Organic materials which are the precursor of graphite usually show low $\delta^{13}C$ values. Organic materials and carbonate minerals exchange carbon isotope between each other during diagenetic and metamorphic processes, and the isotope exchange decreases the $\delta^{13}C$ values of carbonates and increases those of organic materials. However, because of the very low abundance of graphite (<1 vol%), its effect for $\delta^{13}C$ values would be negligible.

Investigated marbles and a carbonate–silicate rock usually contain silicate minerals such as clinopyroxene and grossular garnet, and these minerals can be formed by reactions (1) and (2), respectively. Note that these reactions are decarbonation, which releases CO_2. It has been known that decarbonation reactions in carbonate rocks release CO_2 with heavy C–O (i.e., high $\delta^{13}C$ and $\delta^{18}O$ values) and cause a significant $\delta^{13}C$ decrease and a moderate $\delta^{18}O$ depletion in residual carbonates (Valley, 1986). Therefore, it is plausible to consider that C–O isotope compositions of all investigated samples are affected by decarbonation reactions.

Can the characteristic $\delta^{13}C$ values of Type 5 carbonate–silicate rock be explained by decarbonation reactions? The effect of decarbonation reactions for isotope compositions can be modeled as two end-member processes: "batch model" and "Rayleigh model." The batch model is that all fluids are evolved in a closed system

(i.e., generated fluid stays in a system). On the other hand, the Rayleigh model is the continuous exchange and removal of infinitely small aliquots of fluid, each before the next volatilization (Rumble, 1982; Valley, 1986). These two models are expressed as following equations:

1. Batch model

$$\delta^r_f = \delta^r_i - (1-F)10^3 \ln\alpha_{A-B}$$

2. Rayleigh model

$$\frac{R_f}{R_i} = F^{(\alpha_{A-B}-1)}$$

$$\delta^r_f - \delta^r_i = 10^3 \left(F^{(\alpha_{A-B}-1)} - 1 \right)$$

where R_i and R_f are initial and final isotope ratios of the rock, δ^r_i and δ^r_f are initial and final isotope compositions of the rock (δ notation), F is mole fraction of the element of interest that remains in the rock after reactions, α_{A-B} is the isotope fractionation factor (A: fluid, B: mineral).

We calculated Rayleigh and batch decarbonation models using Chacko et al.'s (1991) fractionation factor at 700 °C. Here, we assumed that the initial $\delta^{18}O$ value ($\delta^{18}O_i$) is +25 ‰, and the initial $\delta^{13}C$ values ($\delta^{13}C_i$) are +4.19 (highest $\delta^{13}C$ values of this study: ms#36), +2, and 0 ‰ (Figures 5 and 8). Regardless of initial $\delta^{13}C$ values, if decarbonation reactions proceed, low $\delta^{13}C$ values of Type 5 carbonate–silicate rock can be explained by the Rayleigh decarbonation process (Figure 8). This is also supported by petrological features such as the fact that Type 5 carbonate–silicate rock is rich in silicate minerals and poor in calcite.
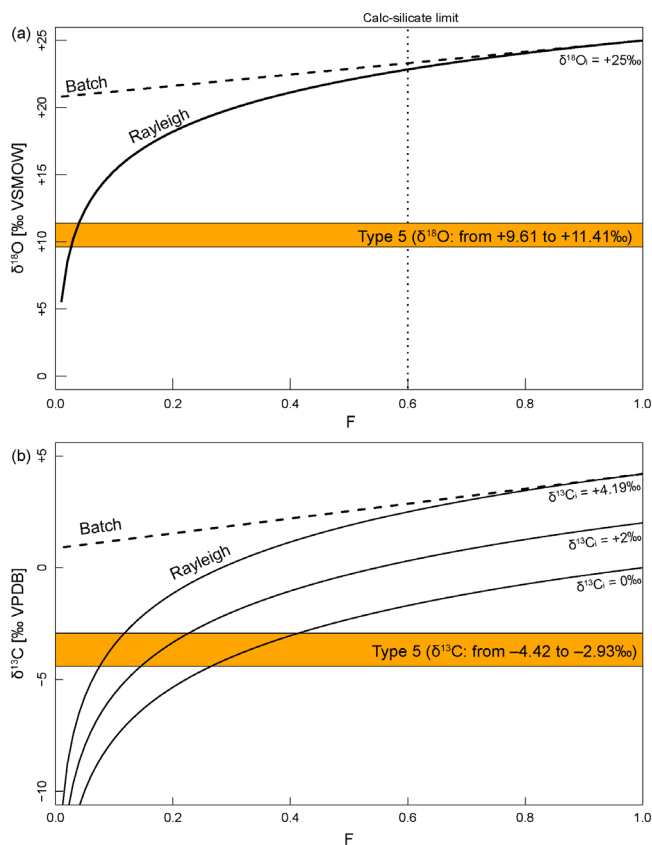
FIGURE 8 Rayleigh and batch decarbonation effects for carbon and oxygen isotope compositions. Using Chacko et al.'s (1991) fractionation factor at $T = 700\,°C$. (a) $\delta^{18}O$ versus F(O) diagram. The initial $\delta^{18}O$ value ($\delta^{18}O_i$) is $+25$ ‰ (based on the Pennsylvanian brachiopod $\delta^{18}O$ values). (b) $\delta^{13}C$ versus F(C) diagram. Assumed initial $\delta^{13}C$ values ($\delta^{13}C_i$) are $+4.19$ (highest $\delta^{13}C$ values of this study: ms#36), $+2$, and 0 ‰

Some analyses of other types of marbles show relatively low $\delta^{13}C$ values (~ 0 ‰), and all types of marbles contain metamorphic clinopyroxenes. Although $\delta^{13}C$ values of Type 1–4 marbles are within the range of marine-carbonate, therefore, decarbonation reactions might have slightly affected the isotope compositions of all samples.

6.2.2 | Isotope exchange with silicate minerals and aqueous fluids

There is a contradiction that the Rayleigh decarbonation model cannot make a large $\delta^{18}O$ shift due to so-called "calc-silicate limit" (Valley, 1986). Thus, other processes to cause a large $\delta^{18}O$ shift are needed.

As $\delta^{18}O$ values of silicate minerals are generally lower than that of marine-carbonate, an isotope exchange between silicate and carbonate minerals is a possible mechanism for $\delta^{18}O$ decrease at the nearly constant $\delta^{13}C$ (e.g., Cook-Kollars et al., 2014; Epstein et al., 2020; Henry et al., 1996; Piccoli et al., 2016). If so, the carbonate–silicate isotope exchange would affect $\delta^{18}O$ values of Type

2 marble, which contains a large amount of silicate minerals. In addition to silicate content, it also depends on the P–T condition and the volume of fluid. In contrast, the carbonate–silicate isotope exchange would have no significant contribution to $\delta^{18}O$ values of Type 1 marble due to its low abundance of silicate minerals. However, Type 1 marble shows a large $\delta^{18}O$ variation and has low $\delta^{18}O$ values (Figure 5). Thus, the oxygen isotope exchange with silicate minerals would not have been a major process to modify $\delta^{18}O$ values of calcites.

An interaction between the marble and externally-infiltrating H_2O-rich fluids during the regional metamorphism can be an alternative hypothesis. Since the isotope fractionation factor becomes smaller at higher temperatures, $\delta^{18}O$ values of marble change to $\delta^{18}O$ values similar to infiltrating fluids at a high-temperature condition. Therefore, the oxygen isotope exchange with low $\delta^{18}O$ hydrothermal fluids (e.g., magmatic fluid) at a high-temperature condition of the regional metamorphism would cause a large decrease in $\delta^{18}O$ values of all types of samples (Figure 5). The $\delta^{18}O$ depletion along the grain-boundary of coarse-grained calcite crystals (1MAHI-1-584.6M: Type 2) supports the fluid infiltrations. It is well known that the H_2O-rich fluid infiltration can cause a large $\delta^{18}O$ shift (e.g., Bickle & Baker, 1990; Nabelek et al., 1984). This process would be a main process to modify $\delta^{18}O$ values of all types of samples. Moreover, high $\delta^{13}C$ values of Type 1 marble suggest that infiltrating aqueous fluids which caused a large $\delta^{18}O$ variation of Type 1 marble did not influence their $\delta^{13}C$ values. Hence, the effect of isotope exchange with fluids for $\delta^{13}C$ values was probably small. One of the possible external fluid sources is the dehydration of hydrous minerals in amphibolitic lithologies associated with marble. Moreover, syn-metamorphic granitic intrusions and the ~ 222 Ma zircon forming fluid infiltration might be a source of magmatic fluids.

Based on the oxygen isotope fractionation factor between H_2O and calcite (e.g., O'Neil et al., 1969; Zheng, 1999), $\delta^{18}O$ values of calcite have to be higher than those of H_2O. Thus, the observed $\delta^{18}O$ values of Type 4 marble cannot be explained by only the isotope exchange with magmatic fluids of igneous $\delta^{18}O$ values ($\sim +5$ ‰). Significantly low $\delta^{18}O$ values of Type 4 marble would be attributed to the interaction with meteoric water with extremely low $\delta^{18}O$ values. Fe-rich clinopyroxenes occur at secondary cracks and have high MnO, which might have correlated to the ore deposit forming metallogenic fluids (Kunugiza, 1999). Shimazaki and Kusakabe (1990) suggested that the Kamioka Mine was formed by the fluid circulation of magmatic and meteoric fluid mixtures. This supports that the infiltration of the ore forming hydrothermal fluids including meteoric water at later stage would have formed the low $\delta^{18}O$ calcites in Type 4 marble.

It is plausible to consider that the interaction between the marbles and externally-infiltrating H_2O-rich fluids made the variation of $\delta^{18}O$ values. However, the pre-metamorphic isotope heterogeneity including the effect of diagenesis and the interaction with meteoric water before the metamorphism cannot be excluded. In fact, it is suggested that some marbles preserve pre-
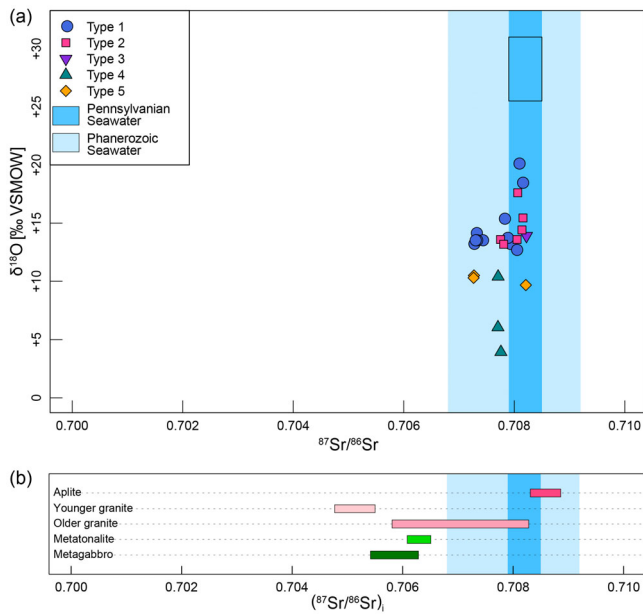
FIGURE 9 (a) Strontium isotope ratios ($^{87}Sr/^{86}Sr$) and oxygen isotope compositions ($\delta^{18}O$) of marble in this study. The black flame shows late Carboniferous (Pennsylvanian) seawater $^{87}Sr/^{86}Sr$ (McArthur et al., 2001) and brachiopod $\delta^{18}O$ ranges (Grossman, 2012). The range of Phanerozoic seawater $^{87}Sr/^{86}Sr$ range is also shown. $^{87}Sr/^{86}Sr$ ratios of marble are plotted within the range of Phanerozoic seawater. (b) $^{87}Sr/^{86}Sr$ ratios of other lithologies in the Hida Belt. Metagabbro, metatonalite and aplite are from the Urushiyama area (Arakawa, 1984). The older granite includes the Yatsuo intrusion (Arakawa, 1990a) and the Hayatsukigawa intrusion (Arakawa, 1990b). The younger granite includes the Okumayama and the Kegachidake intrusions (Arakawa, 1990b). Initial $^{87}Sr/^{86}Sr$ ratios of metagabbro, metatonalite and the older granite are at 222 Ma, those of the younger granite are at 191 Ma (Takahashi et al., 2010) and those of the aplite are at 172 Ma (Arakawa, 1984)

metamorphic C–O isotope signatures (e.g., Boulvais et al., 1998; Rumble et al., 2000).

6.3 | Sr isotope signature

$^{87}Sr/^{86}Sr$ ratios of 10 samples (#S1, #S3, #S4, #S6, #S14, #S15, #S16, #S17, #S18, and #S22) are within the range of Pennsylvanian seawater $^{87}Sr/^{86}Sr$ ratio (McArthur et al., 2001), but those of other samples display lower values. Since the gneissose and granitic rocks in the Hida Belt generally have $^{87}Sr/^{86}Sr$ ratios lower than those of marble in this study (e.g., Arakawa, 1984, 1990a, 1990b) (Figure 9), the effect of external fluids derived from such lithologies may potentially modify the $^{87}Sr/^{86}Sr$ ratios of marble away from the protolith values. However, the $^{87}Sr/^{86}Sr$ ratios of the marble show no clear correlation with the C–O isotopes as well as lithological variations. This suggests that the effect of such fluids was limited, and the observed $^{87}Sr/^{86}Sr$ ratios might be close to their protolith values.

6.4 | Perspectives

In general, decarbonation reactions are induced by a temperature increase and/or a X_{CO_2} decrease (e.g., Bucher & Grapes, 2011; Philpotts & Ague, 2009). In the case of the Hida Belt, some meta-carbonate rocks with a significant modal volume of silicate minerals, such as Type 5 carbonate–silicate rock, show low $\delta^{13}C$ values (~ -5 ‰), whereas other types of samples are within the range of marine-carbonate values ($\sim 0-+4$ ‰). When the carbonates react with silicates under the presence of H_2O-rich aqueous fluids at the condition of upper amphibolite-facies, decarbonation reactions occur and modify $\delta^{13}C$ values of marbles in the Hida Belt. On the other hand, marble with few silicate minerals can retain initial $\delta^{13}C$ values. In any case, the impure features of marble potentially cause a large change in $\delta^{13}C$ values. The large variation of $\delta^{13}C$ values of marble that has been modified by decarbonation reactions during deep continental subduction might affect the carbon isotope heterogeneity in the mantle (e.g., Deines, 1980; Palot et al., 2012; Spetsius et al., 2009, 2017).

The Rayleigh model of decarbonation reactions causes a decrease of carbon (CO_2) content in calcareous rocks as the reaction proceeds. In other words, the decarbonation reactions not only change $\delta^{13}C$ values of carbonate minerals, but also control the input of carbon for the deep carbon cycle. The $\delta^{13}C$ values can change systematically with decreasing bulk carbon contents in carbonate rocks via decarbonation reactions (Valley, 1986). Therefore, if the decarbonation-induced $\delta^{13}C$ change can be approximated quantitatively in orogen-scale, the amount of CO_2 released from the process can be estimated. To further our understanding of the effect of deep subducting marble, a more quantitative approximation on orogen-scale isotope changes is required than that documented in previous studies.

7 | CONCLUSIONS

- C–O isotope analyses of upper amphibolite-facies marbles and a carbonate–silicate rock from the Hida Belt, Japan found a large variation of $\delta^{13}C$ [VPDB] values (from -4.4 to $+4.2$ ‰) and $\delta^{18}O$ [VSMOW] values (from $+1.6$ to $+20.8$ ‰).
- Low $\delta^{13}C$ values of the carbonate–silicate rock (from -4.4 to -2.9 ‰) can be explained by decarbonation (CO_2 releasing) reactions. The occurrence of metamorphic clinopyroxene in all types of samples indicates that all samples have been affected by decarbonation reactions.
- A zircon associated with wollastonite in marble yields U–Pb age of 222.0 ± 3.0 Ma, which likely represents the timing of the recrystallization of marble, triggered by H_2O-rich fluid infiltration at a relatively high-temperature condition.
- The large $\delta^{18}O$ variations can be explained by the isotope exchange via interactions between marble and external magmatic and metamorphic fluids and/or silicates. In addition to these processes, remarkably low $\delta^{18}O$ values (from $+1.6$ to $+13.9$ ‰) of

some marbles would have been affected by the interaction with meteoric water at a later stage.

- Sr isotope ratios ($^{87}Sr/^{86}Sr$ = 0.707255–0.708220) might be close to their protolith values.

ACKNOWLEDGMENTS

ORCID

Hironobu Harada https://orcid.org/0000-0001-5026-3819
Tatsuki Tsujimori https://orcid.org/0000-0001-9202-7312
Keitaro Kunugiza https://orcid.org/0000-0002-2668-4944
Katsuyuki Yamashita https://orcid.org/0000-0001-9127-7889
Shogo Aoki https://orcid.org/0000-0001-5093-1346
Kazumasa Aoki https://orcid.org/0000-0001-7645-6766
Hideko Takayanagi https://orcid.org/0000-0003-3212-9506
Yasufumi Iryu https://orcid.org/0000-0002-6099-0662

REFERENCES

Aoki, S., Aoki, K., Tsuchiya, Y., & Kato, D. (2019). Constraint on the eclogite age of the Sanbagawa metamorphic rocks in central Shikoku, Japan. _International Geology Review_, _61_, 2211–2226.

Aoki, S., Aoki, K., Tsujimori, T., Sakata, S., & Tsuchiya, Y. (2020). Oceanic-arc subduction, stagnation, and exhumation: Zircon U–Pb geochronology and trace-element geochemistry of the Sanbagawa eclogites in central Shikoku, SW Japan. _Lithos_, _358–359_, 105378.

Arakawa, Y. (1984). Rb–Sr ages of the gneiss and metamorphosed intrusive rocks of the Hida metamorphic belt in the Urushiyama area, Gifu Prefecture, central Japan. _The Journal of the Japanese Association of Mineralogists, Petrologists and Economic Geologists_, _79_, 431–442.

Arakawa, Y. (1990a). Two types of granitic intrusions in the Hida belt, Japan: Sr isotopic and chemical characteristics of the Mesozoic Funatsu granitic rocks. _Chemical Geology_, _85_, 101–117.

Arakawa, Y. (1990b). Strontium isotopic compositions of Mesozoic granitic rocks in the Hida belt, central Japan: Diversities of magma sources and of processes of magma evolution in a continental margin area. _Lithos_, _24_, 261–273.

Arita, Y., & Wada, H. (1990). Stable isotopic evidence for migration of metamorphic fluids along grain boundaries of marbles. _Geochemical Journal_, _24_, 173–186.

Asami, M. (1979). Pelitic metamorphic rocks from Arashima-dake area, Toga area and Wada-gawa area of the Hida metamorphic belt. _The Basement of Japanese Islands (Professor Kano Memorial Volume)_, 41–49 (in Japanese with English abstract).

Baba, K., & Yoshida, T. (2020). Geological structures controlled the rupture process of the 2011 M9.0 Tohoku-Oki earthquake in the Northeast Japan Arc. _Earth, Planets and Space_, _72_, 1–14.

Bickle, M. J., & Baker, J. (1990). Advective-diffusive transport of isotopic fronts: An example from Naxos, Greece. _Earth and Planetary Science Letters_, _97_, 78–93.

Boulvais, P., Fourcade, S., Gruau, G., Moine, B., & Cuney, M. (1998). Persistence of pre-metamorphic C and O isotopic signatures in marbles subject to Pan-African granulite-facies metamorphism and U–Th mineralization (Tranomaro, Southeast Madagascar). _Chemical Geology_, _150_, 247–262.

Bucher, K., & Grapes, R. (2011). _Petrogenesis of metamorphic rocks_. Berlin: Springer.

Castelli, D. (1991). Eclogitic metamorphism in carbonate rocks: The example of impure marbles from the Sesia-Lanzo Zone, Italian Western Alps. _Journal of Metamorphic Geology_, _9_, 61–77.

Chacko, T., Mayeda, T. K., Clayton, R. N., & Goldsmith, J. R. (1991). Oxygen and carbon isotope fractionations between CO_2 and calcite. _Geochimica et Cosmochimica Acta_, _55_, 2867–2882.

Cook-Kollars, J., Bebout, G. E., Collins, N. C., Angiboust, S., & Agard, P. (2014). Subduction zone metamorphic pathway for deep carbon cycling: I. Evidence from HP/UHP metasedimentary rocks, Italian Alps. _Chemical Geology_, _386_, 31–48.

Coplen, T. B., Kendall, C., & Hopple, J. (1983). Comparison of stable isotope reference samples. _Nature_, _302_, 236–238.

Corfu, F., Hanchar, J. M., Hoskin, P. W., & Kinny, P. (2003). Atlas of zircon textures. _Reviews in Mineralogy and Geochemistry_, _53_, 469–500.

Deines, P. (1980). The carbon isotopic composition of diamonds: Relationship to diamond shape, color, occurrence and vapor composition. _Geochimica et Cosmochimica Acta_, _44_, 943–961.

Ehiro, M., Tsujimori, T., Tsukada, K., & Nuramkhaan, M. (2016). Paleozoic basement and associated cover. In T. Moreno, S. Wallis, T. Kojima, & W. Gibbons (Eds.), _The geology of Japan_ (pp. 25–60). London, England: Geological Society.

Epstein, G. S., Bebout, G. E., Angiboust, S., & Agard, P. (2020). Scales of fluid-rock interaction and carbon mobility in the deeply underplated and HP-Metamorphosed Schistes Lustrés, Western Alps. _Lithos_, _354–355_, 105229.

Ernst, W. G. (1974). Metamorphism and ancient continental margins. In C. A. Burk & C. L. Drake (Eds.), _The geology of continental margins_ (pp. 907–919). Springer: Berlin.

Ernst, W. G., Tsujimori, T., Zhang, R., & Liou, J. G. (2007). Permo-Triassic collision, subduction-zone metamorphism, and tectonic exhumation along the East Asian continental margin. _Annual Review of Earth and Planetary Sciences_, _35_, 73–110.

Ganbat, A., Tsujimori, T., Boniface, N., Pastor-Galán, D., Aoki, S., & Aoki, K. (2021). Crustal evolution of the Paleoproterozoic Ubendian Belt (SW Tanzania) western margin: A Central African Shield amalgamation tale. _Gondwana Research_, _91_, 286–306.

Geng, Y. S. (2015). Early Precambrian geological signatures in South China craton. In M. G. Zhai (Ed.), _Precambrian geology of China_ (pp. 207–240). Berlin: Springer.

Gerdes, M. L., Baumgartner, L. P., Person, M., & Rumble, D. (1995). One- and two-dimensional models of fluid flow and stable isotope exchange at an outcrop in the Adamello contact aureole, Southern Alps, Italy. _American Mineralogist_, _80_, 1004–1019.

Graham, C. M., Valley, J. W., Eiler, J. M., & Wada, H. (1998). Timescales and mechanisms of fluid infiltration in a marble: An ion microprobe study. _Contributions to Mineralogy and Petrology_, _132_, 371–389.

Grossman, E. L. (2012). Oxygen isotope stratigraphy. In F. M. Gradstein, J. G. Ogg, M. D. Schmitz, & G. M. Ogg (Eds.), _The geologic time scale 2012_ (Vol. 1, pp. 181–206). Amsterdam: Elsevier.

Henry, C., Burkhard, M., & Goffé, B. (1996). Evolution of synmetamorphic veins and their wallrocks through a Western Alps transect: No evidence for large-scale fluid flow. Stable isotope, major-and trace-element systematics. _Chemical Geology_, _127_, 81–109.

Hiroi, Y. (1981). Subdivision of the Hida metamorphic complex, central Japan, and its bearing on the geology of the Far East in pre-Sea of Japan time. _Tectonophysics_, _76_, 317–333.

Hiroi, Y., Fuji, N., & Okimura, Y. (1978). New fossil discovery from the Hida metamorphic rocks in the Unazuki area, central Japan. _Proceedings of the Japan Academy, Series B_, _54_, 268–271.

Horie, K., Takehara, M., Suda, Y., & Hidaka, H. (2013). Potential Mesozoic reference zircon from the Unazuki plutonic complex: Geochronological and geochemical characterization. _Island Arc_, _22_, 292–305.

Horie, K., Tsutsumi, Y., Takehara, M., & Hidaka, H. (2018). Timing and duration of regional metamorphism in the Kagasawa and Unazuki areas, Hida metamorphic complex, southwest Japan. *Chemical Geology*, *484*, 148–167.

Horie, K., Yamashita, M., Hayasaka, Y., Katoh, Y., Tsutsumi, Y., Katsube, A., Hidaka, H., Kim, H., & Cho, M. (2010). Eoarchean–Paleoproterozoic zircon inheritance in Japanese Permo-Triassic granites (Unazuki area, Hida Metamorphic Complex): Unearthing more old crust and identifying source terranes. *Precambrian Research*, *183*, 145–157.

Imai, N., Ogasawara, Y., Wakabayashi, N., & Terao, Y. (1977). Carbonate rocks in the Hida Metamorphic Belts with special reference to the intergrowths of dolomite and the cementing magnesian calcite (preliminary report). Preliminary remarks to the petrology on the calcareous gneisses and metamorphic carbonate rocks in the Hida Metamorphic Belts, Central Japan. *Bulletin of Science and Engineering Research Laboratory*, *Waseda University*, *78*, 26–42 (in Japanese with English abstract).

Isozaki, Y. (1996). Anatomy and genesis of a subduction-related orogen: A new view of geotectonic subdivision and evolution of the Japanese Islands. *Island Arc*, *5*, 289–320.

Isozaki, Y. (1997). Contrasting two types of orogen in Permo-Triassic Japan: Accretionary versus collisional. *Island Arc*, *6*, 2–24.

Isozaki, Y. (2019). A visage of early Paleozoic Japan: Geotectonic and paleobiogeographical significance of Greater South China. *Island Arc*, *28*, e12296.

Isozaki, Y., Aoki, K., Nakama, T., & Yanai, S. (2010). New insight into a subduction-related orogen: A reappraisal of the geotectonic framework and evolution of the Japanese Islands. *Gondwana Research*, *18*, 82–105.

Isozaki, Y., Aoki, K., Sakata, S., & Hirata, T. (2014). The eastern extension of Paleozoic South China in NE Japan evidenced by detrital zircon. *GFF*, *136*, 116–119.

Isozaki, Y., Ehiro, M., Nakahata, H., Aoki, K., Sakata, S., & Hirata, T. (2015). Cambrian plutonism in Northeast Japan and its significance for the earliest arc-trench system of proto-Japan: New U–Pb zircon ages of the oldest granitoids in the Kitakami and Ou Mountains. *Journal of Asian Earth Sciences*, *108*, 136–149.

Isozaki, Y., Nakahata, H., Zakharov, Y. D., Popov, A. M., Sakata, S., & Hirata, T. (2017). Greater South China extended to the Khanka block: Detrital zircon geochronology of middle-upper Paleozoic sandstones in Primorye, Far East Russia. *Journal of Asian Earth Sciences*, *145*, 565–575.

Jin, F., & Ishiwatari, A. (1997). Petrological and geochemical study on Hida gneisses in the upper reach area of Tetori river: Comparative study on the pelitic metamorphic rocks with the other areas of Hida belt, Sino-Korean block and Yangtze block. *Journal of Mineralogy, Petrology and Economic Geology*, *92*, 213–230 (in Japanese with English abstract).

Kano, T. (1973). Geological study of the Hida metamorphic belt in the eastern part of Toyama Prefecture, Central Japan (part 1): On the tectonic division, the characteristics of the Funatsu stage plutonism, and the lithostratigraphic division of the metamorphic rocks. *The Journal of the Geological Society of Japan*, *79*, 407–421 (in Japanese with English abstract).

Kano, T. (1982). Tectonic divisions and their developmment of the Hida metamorphic region, central Japan. *The Memoirs of the Geological Society of Japan*, *21*, 9–24 (in Japanese with English abstract).

Kano, T. (1983). Origin of augen gneisses and related mylonitic rocks in the eastern part of the Hida metamorphic region, central Japan. (part 1): Mode of occurrences, petrographical and mineralogical properties of rocks and potash-feldspar megacrysts. *The Journal of the Geological Society of Japan*, *89*, 375–393 (in Japanese with English abstract).

Kano, T. (1990a). Intrusive relation of the Okumayama Granitic Mass (Shimonomoto type) into the Iori Granitic Mass (Funatsu type) in the hayatsukigawa area: Re-examination of the sub-division for early Mesozoic granites (Funatsu Granites) in the Hida region. *The Journal of Geological Society of Japan*, *96*, 379–388 (in Japanese with English abstract).

Kano, T. (1990b). Granitic rocks in the Hida complex. *Mining Geology*, *40*, 397–413 (in Japanese with English abstract).

Kano, T. (1998). Crystalline limestone in the Hida metamorphic complex, central Japan – Geological characteristics, mineral compositions, texture and mode of occurrences of dolomite. *Shigen-Chishitsu*, *48*, 77–92 (in Japanese with English abstract).

Kano, T., & Watanabe, T. (1995). Geology and structure of the early Mesozoic granitoids in the east of the Kamioka mining area, southern Hida metamorphic region, central Japan. *The Journal of Geological Society of Japan*, *101*, 499–514 (in Japanese with English abstract).

Kato, T., Enami, M., & Zhai, M. (1997). Ultra-high-pressure (UHP) marble and eclogite in the Su–Lu UHP terrane, eastern China. *Journal of Metamorphic Geology*, *15*, 169–182.

Khanchuk, A. I., Kemkin, I. V., & Kruk, N. N. (2016). The Sikhote-Alin orogenic belt, Russian South East: Terranes and the formation of continental lithosphere based on geological and isotopic data. *Journal of Asian Earth Sciences*, *120*, 117–138.

Kim, S. W., Kee, W. S., Santosh, M., Cho, D. L., Hong, P. S., Ko, K., Lee, B. C., Byun, U. H., & Jang, Y. (2020). Tracing the Precambrian tectonic history of East Asia from Neoproterozoic sedimentation and magmatism in the Korean Peninsula. *Earth-Science Reviews*, *209*, 103311.

Koizumi, S., & Otoh, S. (2020) The Permian–Triassic plutonic and metamorphic rocks in the Saragawa–Bandojima area, Katsuyama City, Fukui Prefecture, central Japan. *Katsuyama City Geopark Academic Research Encouragement Project Academic Research Report*, p. 18 (in Japanese with English abstract).

Komatsu, M., Nagase, M., Naito, K., Kanno, T., Ujihara, M., & Toyoshima, T. (1993). Structure and tectonics of the Hida massif, central Japan. *Memoir of the Geological Society of Japan*, *42*, 39–62 (in Japanese with English abstract).

Kunugiza, K. (1999). Incipient stage of ore formation process of the Kamioka Zn–Pb ore deposit in the Hida metamorphic belt, central Japan: Leaching and precipitation of clinopyroxene. *Resource Geology*, *49*, 199–212.

Kunugiza, K., & Kaneko, K. (2001). *Metamorphic rocks and granites of the eastern Hida Belt*, *Toyama Prefecture*. Field Guidebook, no. 10, 108th Annual Meeting of Geological Society of Japan (Kanazawa), pp. 1–20 (in Japanese).

Kunugiza, K., Shimizu, M., & Otoh, S. (2010). U–Th–Pb chronological constraints on the geotectonic history of central Japan from the Hida metamorphism through the opening of Japan to the present. *Journal of the Geological Society of Japan*, *116*(Suppl.), 83–101 (in Japanese).

Liou, J. G., Tsujimori, T., Zhang, R. Y., Katayama, I., & Maruyama, S. (2004). Global UHP metamorphism and continental subduction/collision: The Himalayan model. *International Geology Review*, *46*, 1–27.

Liu, P., Wu, Y., Chen, Y., Zhang, J., & Jin, Z. (2015). UHP impure marbles from the Dabie Mountains: Metamorphic evolution and carbon cycling in continental subduction zones. *Lithos*, *212–215*, 280–297.

Maruyama, S. (1997). Pacific-type orogeny revisited: Miyashiro-type orogeny proposed. *Island Arc*, *6*, 91–120.

Maruyama, S., Isozaki, Y., Kimura, G., & Terabayashi, M. (1997). Paleogeographic maps of the Japanese Islands: Plate tectonic synthesis from 750 Ma to the present. *Island Arc*, *6*, 121–142.

Maruyama, S., Liou, J. G., & Terabayashi, M. (1996). Blueschists and eclogites of the world and their exhumation. *International Geology Review*, *38*, 485–594.

McAleer, R. J., Jubb, A. M., Hackley, P. C., Walsh, G. J., Merschat, A. J., Regan, S. P., Burton, W. C., & Vazquez, J. A. (2020). Photoluminescence imaging of whole zircon grains on a petrographic microscope—An underused aide for geochronologic studies. *Minerals*, *10*, 876.

McArthur, J. M., Howarth, R. J., & Bailey, T. R. (2001). Strontium isotope stratigraphy: LOWESS version 3: Best fit to the marine Sr-isotope curve for 0–509 Ma and accompanying look-up table for deriving numerical age. *The Journal of Geology*, 109, 155–170.

Metal Mining Agency of Japan. (1995). *Report of detailed geological survey; the Hida region, 1994 fiscal year* (in Japanese).

Ministry of International Trade and Industry, Agency for Natural Resources and Energy. (1989). *Report of regional survey; Projects for structural analysis, 1988 fiscal year* (in Japanese).

Ministry of International Trade and Industry, Agency for Natural Resources and Energy. (1992). *Report of regional geological survey; The Hida region, 1991 fiscal year* (in Japanese).

Ministry of International Trade and Industry, Agency for Natural Resources and Energy. (1993). *Report of regional geological survey; The Hida region, 1992 fiscal year* (in Japanese).

Ministry of International Trade and Industry, Agency for Natural Resources and Energy. (1996). *Report of regional geological survey; Projects for structural analysis, 1995 fiscal year* (in Japanese).

Ministry of International Trade and Industry, Agency for Natural Resources and Energy. (1997). *Report of regional geological survey; Projects for structural analysis, 1996 fiscal year* (in Japanese).

Ministry of International Trade and Industry, Agency for Natural Resources and Energy. (1998a). *Report of regional geological survey; the Hida region, 1997 fiscal year* (in Japanese).

Ministry of International Trade and Industry, Agency for Natural Resources and Energy. (1998b). *Report of regional geological survey; Projects for structural analysis, 1997 fiscal year* (in Japanese).

Ministry of International Trade and Industry, Agency for Natural Resources and Energy. (1999). *Report of regional geological survey; The Hida region, 1998 fiscal year* (in Japanese).

Ministry of International Trade and Industry, Agency for Natural Resources and Energy. (2000). *Report of regional geological survey; The Hida region, 1998 fiscal year* (in Japanese).

Morishita, Y. (1999). Three-dimensional isotopic characteristics of crystalline limestone around the Sakonishi Zn ore bodies in the Kamioka mining district, Japan. *Resource Geology*, 49, 243–257.

Nabelek, P. I., Labotka, T. C., O'Neil, J. R., & Papike, J. J. (1984). Contrasting fluid/rock interaction between the Notch Peak granitic intrusion and argillites and limestones in western Utah: Evidence from stable isotopes and phase assemblages. *Contributions to Mineralogy and Petrology*, 86, 25–34.

Nabelek, P. I., & Morgan, S. S. (2012). Metamorphism and fluid flow in the contact aureole of the Eureka Valley–Joshua Flat–Beer Creek pluton, California. *Geological Society of America Bulletin*, 124, 228–239.

Nagasawa, K., & Shibata, K. (1985). K–Ar ages of sericites from the Kamioka mine and its significance in geochronology of the Kamioka deposits. *Mining Geology*, 35, 57–65 (in Japanese with English abstract).

Nakano, T., Murakami, H., Miyake, K., & Nakayama, K. (1997). Chemical composition of ^{18}O-depleted limestone in the Kamioka Zn–Pb mine. *Resource Geology*, 47, 109–119.

Nozawa, T. (1952). On the genesis of Inishi syenitic rock. *The Journal of Geological Society of Japan*, 58, 469–475 (in Japanese).

Ogasawara, Y., Ohta, M., Fukasawa, K., Katayama, I., & Maruyama, S. (2000). Diamond-bearing and diamond-free metacarbonate rocks from Kumdy–Kol in the Kokchetav Massif, northern Kazakhstan. *Island Arc*, 9, 400–416.

Ohta, M., Mock, T., Ogasawara, Y., & Rumble, D. (2003). Oxygen, carbon, and strontium isotope geochemistry of diamond-bearing carbonate rocks from Kumdy-Kol, Kokchetav Massif, Kazakhstan. *Lithos*, 70, 77–90.

Omori, S., Liou, J. G., Zhang, R. Y., & Ogasawara, Y. (1998). Petrogenesis of impure dolomitic marble from the Dabie Mountains, central China. *Island Arc*, 7, 98–114.

Omori, S., & Mariko, T. (1999). Physicochemical environment during the formation of the Mozumi skarn-type Pb–Zn–Ag deposit at the Kamioka Mine, central Japan: A thermochemical study. *Resource Geology*, 49, 223–232.

O'Neil, J. R., Clayton, R. N., & Mayeda, T. K. (1969). Oxygen isotope fractionation in divalent metal carbonates. *The Journal of Chemical Physics*, 51, 5547–5558.

Palot, M., Cartigny, P., Harris, J. W., Kaminsky, F. V., & Stachel, T. (2012). Evidence for deep mantle convection and primordial heterogeneity from nitrogen and carbon stable isotopes in diamond. *Earth and Planetary Science Letters*, 357, 179–193.

Philpotts, A., & Ague, J. (2009). *Principles of igneous and metamorphic petrology*. Cambridge: Cambridge University Press.

Piccoli, F., Brovarone, A. V., Beyssac, O., Martinez, I., Ague, J. J., & Chaduteau, C. (2016). Carbonation by fluid–rock interactions at high-pressure conditions: Implications for carbon cycling in subduction zones. *Earth and Planetary Science Letters*, 445, 146–159.

Proyer, A., Mposkos, E., Baziotis, I., & Hoinkes, G. (2008). Tracing high-pressure metamorphism in marbles: Phase relations in high-grade aluminous calcite–dolomite marbles from the Greek Rhodope massif in the system $CaO–MgO–Al_2O_3–SiO_2–CO_2$ and indications of prior aragonite. *Lithos*, 104, 119–130.

Roselle, G. T., Baumgartner, L. P., & Valley, J. W. (1999). Stable isotope evidence of heterogeneous fluid infiltration at the Ubehebe Peak contact aureole, Death Valley National Park, California. *American Journal of Science*, 299, 93–138.

Rumble, D., III. (1982). Stable isotope fractionation during metamorphic devolatilization reactions. *Reviews in Mineralogy and Geochemistry*, 10, 327–353.

Rumble, D., III, Wang, Q., & Zhang, R. (2000). Stable isotope geochemistry of marbles from the coesite UHP terrains of Dabieshan and Sulu, China. *Lithos*, 52, 79–95.

Sakoda, M., Kano, T., Fanning, C. M., & Sakaguchi, T. (2006). SHRIMP U–Pb zircon age of the Inishi migmatite around the Kamioka mining area, Hida metamorphic complex, central Japan. *Resource Geology*, 56, 17–26.

Sakurai, W., Okada, Y., & Mizuyachi, O. (1993). On the exploration of the Atotsugawa district in the Kamioka mining area. *Shigen-Chishitsu*, 43, 79–91.

Saltzman, M. R., & Thomas, E. (2012). Carbon isotope stratigraphy. In F. M. Gradstein, J. G. Ogg, M. D. Schmitz, & G. M. Ogg (Eds.), *The geologic time scale 2012* (Vol. 1, pp. 207–232). Amsterdam: Elsevier.

Sano, S. I., & Yabe, A. (2017). Fauna and flora of Early Cretaceous Tetori Group in Central Japan: The clues to revealing the evolution of Cretaceous terrestrial ecosystem in East Asia. *Palaeoworld*, 26, 253–267.

Sano, Y., Hidaka, H., Terada, K., Shimizu, H., & Suzuki, M. (2000). Ion microprobe U–Pb zircon geochronology of the Hida gneiss: Finding of the oldest minerals in Japan. *Geochemical Journal*, 34, 135–153.

Satish-Kumar, M., Hermann, J., Miyamoto, T., & Osanai, Y. (2010). Fingerprinting a multistage metamorphic fluid–rock history: Evidence from grain scale Sr, O and C isotopic and trace element variations in high-grade marbles from East Antarctica. *Lithos*, 114, 217–228.

Sato, K., & Uchiumi, S. (1990). K–Ar ages and mineralization of Kamioka Pb–Zn skarn deposit in the Hida terrain. *Mining Geology*, 40, 389–396 (in Japanese with English abstract).

Schumacher, J. C., Brady, J. B., Cheney, J. T., & Tonnsen, R. R. (2008). Glaucophane-bearing marbles on Syros, Greece. *Journal of Petrology*, 49, 1667–1686.

Shimazaki, H., & Kusakabe, M. (1990). Oxygen isotope study of the Kamioka Zn–Pb skarn deposits, central Japan. *Mineralium Deposita*, 25, 221–229.

Sohma, T., & Akiyama, S. (1984). Geological structure and lithofacies in the central part of the Hida metamorphic belt. *The Journal of Geological Society of Japan*, 90, 609–628 (in Japanese with English abstract).

Sohma, T., & Kunugiza, K. (1993). The formation of the Hida nappe and the tectonics of Mesozoic sediments: The tectonic evolution of the Hida region, Central Japan. *Memoirs of the Geological Society of Japan*, *42*, 1–20 (in Japanese with English abstract).

Spetsius, Z. V., Cliff, J., Griffin, W. L., & O'Reilly, S. Y. (2017). Carbon isotopes of eclogite-hosted diamonds from the Nyurbinskaya kimberlite pipe, Yakutia: The metasomatic origin of diamonds. *Chemical Geology*, *455*, 131–147.

Spetsius, Z. V., de Vries, D. W., & Davies, G. R. (2009). Combined C isotope and geochemical evidence for a recycled origin for diamondiferous eclogite xenoliths from kimberlites of Yakutia. *Lithos*, *112*, 1032–1042.

Suwa, K., Shiozaki, H., Sohma, T., Asami, M., Kano, T., Hoshino, M., & Suzuki, M. (1981). Hida metamorphic rocks and plutonic rocks in the Wada-gawa and Oguchi-gawa area, southeastern part of Toyama Prefecture, central Japan. *The Journal of the Geological Society of Japan*, *87*, 143–155 (in Japanese with English abstract).

Suzuki, M. (1959). Metasomatic replacement of crystalline limestones found in the Mizunashi District, Western part of the Hida metamorphic zone. *The Journal of the Geological Society of Japan*, *65*, 184–195 (in Japanese with English abstract).

Suzuki, M., Nakazawa, S., & Osakabe, T. (1989). Tectonic development of the Hida Belt: With special reference to its metamorphic history and late Carboniferous to Triassic orogenies. *Memoirs of the Geological Society of Japan*, *33*, 1–10 (in Japanese with English abstract).

Takahashi, Y., Cho, D. L., & Kee, W. S. (2010). Timing of mylonitization in the Funatsu Shear Zone within Hida Belt of southwest Japan: Implications for correlation with the shear zones around the Ogcheon Belt in the Korean Peninsula. *Gondwana Research*, *17*, 102–115.

Takahashi, Y., Cho, D. L., Mao, J., Zhao, X., & Yi, K. (2018). SHRIMP U–Pb zircon ages of the Hida metamorphic and plutonic rocks, Japan: Implications for late Paleozoic to Mesozoic tectonics around the Korean Peninsula. *Island Arc*, *27*, e12220.

Takehara, M., & Horie, K. (2019). U–Pb zircon geochronology of the Hida gneiss and granites in the Kamioka area, Hida Belt. *Island Arc*, *28*, e12303.

Tang, J., Zheng, Y. F., Wu, Y. B., & Gong, B. (2006). Zircon SHRIMP U–Pb dating, C and O isotopes for impure marbles from the Jiaobei terrane in the Sulu orogen: Implication for tectonic affinity. *Precambrian Research*, *144*, 1–18.

Tsujimori, T. (1995). Staurolite-bearing sillimanite schist cobble from the Upper Jurassic Tetori Group in the Kuzuryu area, Hida Mountains, Central Japan. *The Journal of Geological Society of Japan*, *101*, 971–977.

Tsujimori, T. (2002). Prograde and retrograde PT paths of the late Paleozoic glaucophane eclogite from the Renge metamorphic belt, Hida Mountains, southwestern Japan. *International Geology Review*, *44*, 797–818.

Tsujimori, T., & Liou, J. G. (2005). Eclogite-facies mineral inclusions in clinozoisite from Paleozoic blueschist, central Chugoku Mountains, southwest Japan: Evidence of regional eclogite-facies metamorphism. *International Geology Review*, *47*, 215–232.

Valley, J. (1986). Stable isotope geochemistry of metamorphic rocks. *Reviews in Mineralogy and Geochemistry*, *16*, 445–489.

Vermeesch, P. (2018). IsoplotR: A free and open toolbox for geochronology. *Geoscience Frontiers*, *9*, 1479–1493.

Wada, H. (1977). Isotopic studies of graphite in metamorphosed carbonate rocks of central Japan. *Geochemical Journal*, *11*, 183–197.

Wada, H. (1988). Microscale isotopic zoning in calcite and graphite crystals in marble. *Nature*, *331*, 61–63.

Wakita, K. (2013). Geology and tectonics of Japanese islands: A review – The key to understanding the geology of Asia. *Journal of Asian Earth Sciences*, *72*, 75–87.

Wan, H., Xiao, Y., Sun, H., Liu, H., Wang, Y., Li, D., & Li, W. (2020). The lithium isotopic composition and geochemical implication of ultrahigh-pressure marbles from the Dabie–Sulu orogen, China. *Journal of Asian Earth Sciences*, *195*, 104376.

Whitney, D. L., & Evans, B. W. (2010). Abbreviations for names of rock-forming minerals. *American Mineralogist*, *95*, 185–187.

Xu, J., Ben-Avraham, Z., Kelty, T., & Yu, H. S. (2014). Origin of marginal basins of the NW Pacific and their plate tectonic reconstructions. *Earth-Science Reviews*, *130*, 154–196.

Yanai, S., Aoki, K., & Akahori, Y. (2010). Opening of Japan Sea and major tectonic lines of Japan: MTL, TTL and Fossa Magna. *Journal of Geography*, *119*, 1079–1124 (in Japanese with English abstract).

Yao, J., Cawood, P. A., Shu, L., & Zhao, G. (2019). Jiangnan Orogen, South China: A ∼970–820 Ma Rodinia margin accretionary belt. *Earth-Science Reviews*, *196*, 102872.

Yoshida, S., Ishikawa, A., Aoki, S., & Komiya, T. (2021). Occurrence and chemical composition of the Eoarchean carbonate rocks of the Nulliak supracrustal rocks in the Saglek Block of northeastern Labrador, Canada. *Island Arc*, *30*, e12381.

Yui, T. F., & Fukuyama, M. (2015). A revisit to the Yorii jadeite–quartz rock, the Kanto Mountains, central Japan: Implications for petrogenesis. *Journal of Asian Earth Sciences*, *108*, 58–67.

Yui, T. F., Fukuyama, M., Iizuka, Y., Wu, C. M., Wu, T. W., Liou, J. G., & Grove, M. (2013). Is Myanmar jadeitite of Jurassic age? A result from incompletely recrystallized inherited zircon. *Lithos*, *160*, 268–282.

Zhai, M., Zhang, X. H., Zhang, Y. B., Wu, F. Y., Peng, P., Li, Q. L., Li, Z., Guo, J., Li, T.-S., Zhao, L., Zhou, L. G., & Zhu, X. (2019). The geology of North Korea: An overview. *Earth-Science Reviews*, *194*, 57–96.

Zhang, D., Liu, Y. J., Li, W. M., Li, S. Z., Iqbal, M. Z., & Chen, Z. X. (2020). Marginal accretion processes of Jiamusi Block in NE China: Evidences from detrital zircon U–Pb age and deformation of the Wandashan Terrane. *Gondwana Research*, *78*, 92–109.

Zhao, G., Sun, M., Wilde, S. A., & Sanzhong, L. (2005). Late Archean to Paleoproterozoic evolution of the North China Craton: Key issues revisited. *Precambrian Research*, *136*, 177–202.

Zhao, G., Wilde, S. A., Cawood, P. A., & Sun, M. (2001). Archean blocks and their boundaries in the North China Craton: Lithological, geochemical, structural and P–T path constraints and tectonic evolution. *Precambrian Research*, *107*, 45–73.

Zhao, G., & Zhai, M. (2013). Lithotectonic elements of Precambrian basement in the North China Craton: Review and tectonic implications. *Gondwana Research*, *23*, 1207–1240.

Zhao, X., Mao, J., Ye, H., Liu, K., & Takahashi, Y. (2013). New SHRIMP U–Pb zircon ages of granitic rocks in the Hida Belt, Japan: Implications for tectonic correlation with Jiamushi massif. *Island Arc*, *22*, 508–521.

Zheng, Y. F. (1999). Oxygen isotope fractionation in carbonate and sulfate minerals. *Geochemical Journal*, *33*, 109–126.

Zhou, J. B., & Li, L. (2017). The Mesozoic accretionary complex in Northeast China: Evidence for the accretion history of Paleo-Pacific subduction. *Journal of Asian Earth Sciences*, *145*, 91–100.

SUPPORTING INFORMATION

Additional supporting information may be found online in the Supporting Information section at the end of this article.

FIGURE S1

30
3.61
18.95

29   27
3.47   3.55
17.33   19.13   28
                     3.55
S4   20.25
3.53
18.46
0.708136

26   25   24
3.54   3.47   3.54
18.16   18.21   18.40

31
2.87
14.77

35
3.29
18.07

32   33   34
3.62   3.56   3.66
19.37   18.02   16.90

2 cm

42
1.62
15.93

43   S25
2.53   1.39
15.39   15.41

36   S26
4.19   2.17   S5
20.82   16.16   1.78
                                                      15.29
        37   38   39   40   0.707807
        3.27   2.80   2.62   2.31
        18.77   17.50   17.82   16.35   41
S6   2.14
3.63   16.33
20.13
0.708071
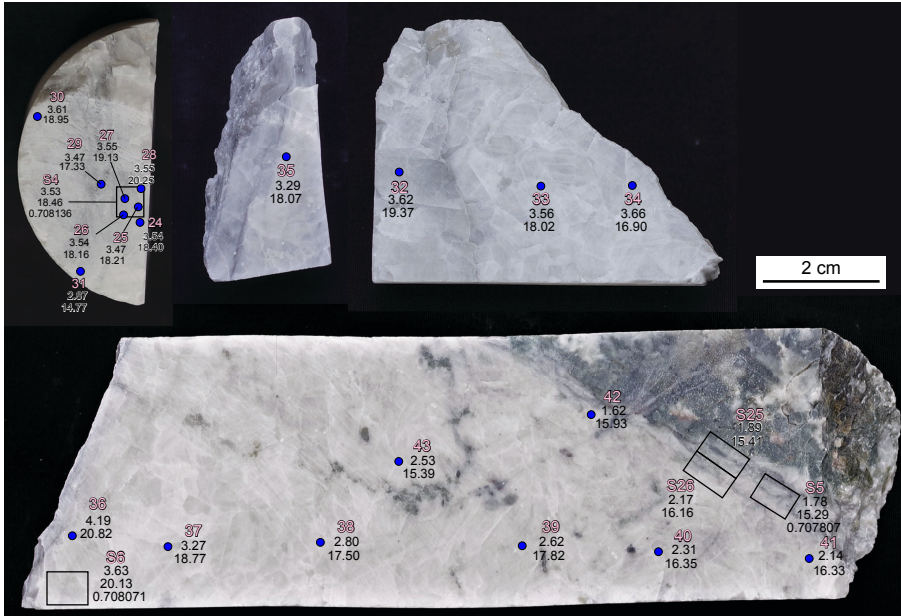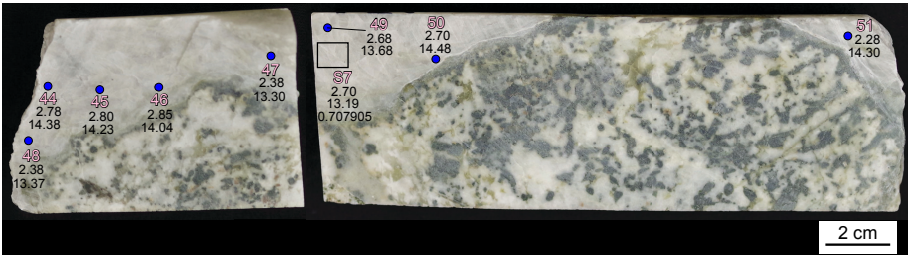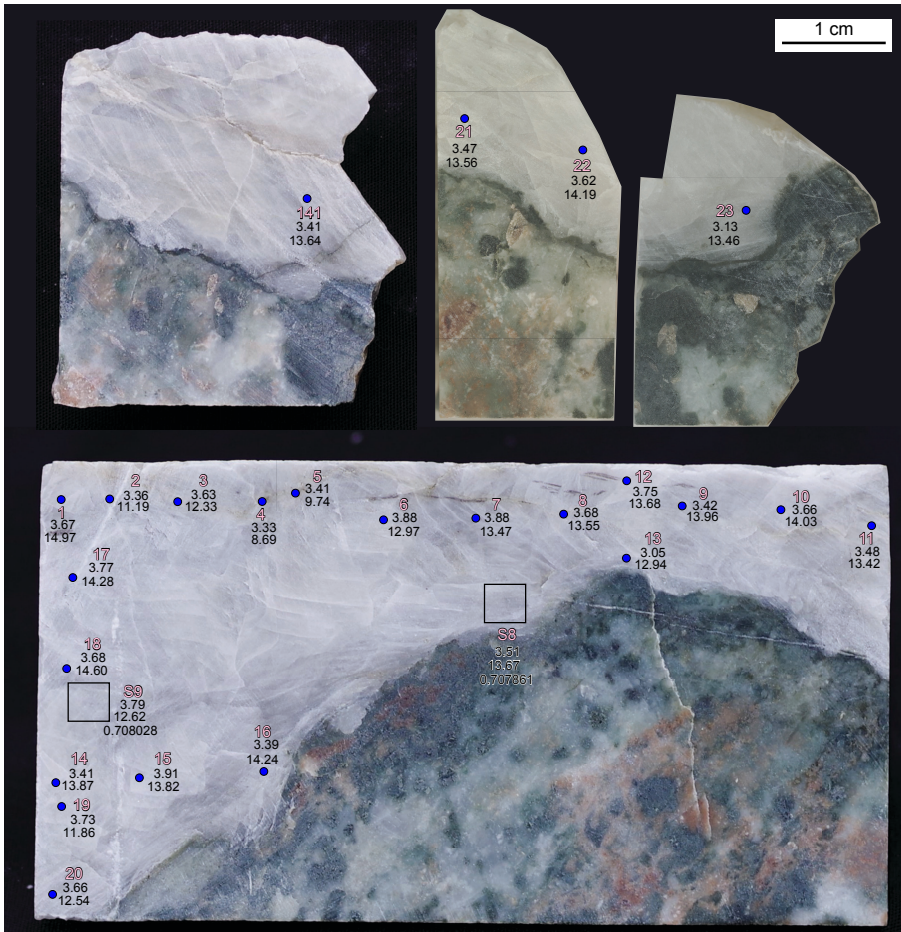
FIGURE S2

FIGURE S3

FIGURE S4
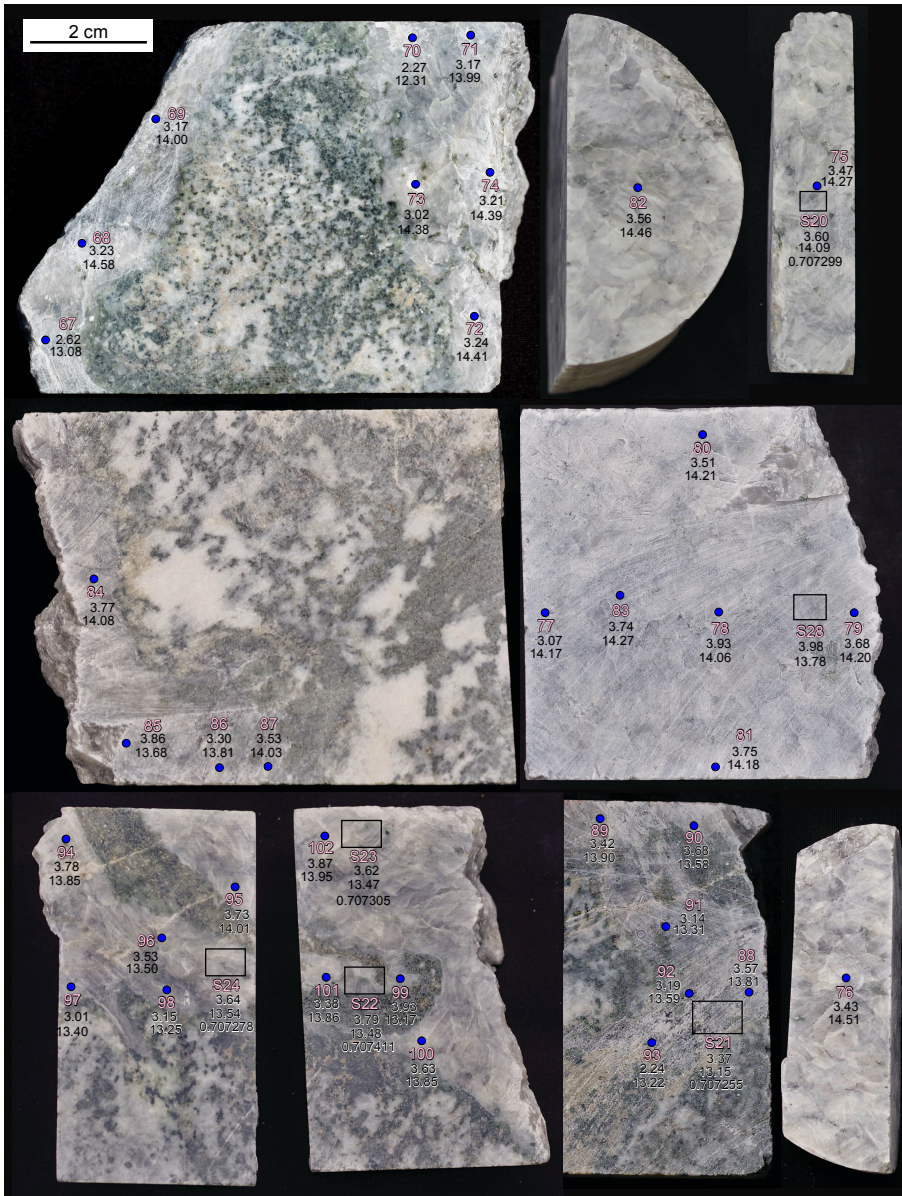
FIGURE S5

FIGURE S6

FIGURE S7

52
-0.25
14.10

S16
-0.01
13.95
0.708220

139
0.82
14.31

140
1.11
14.15

1 cm
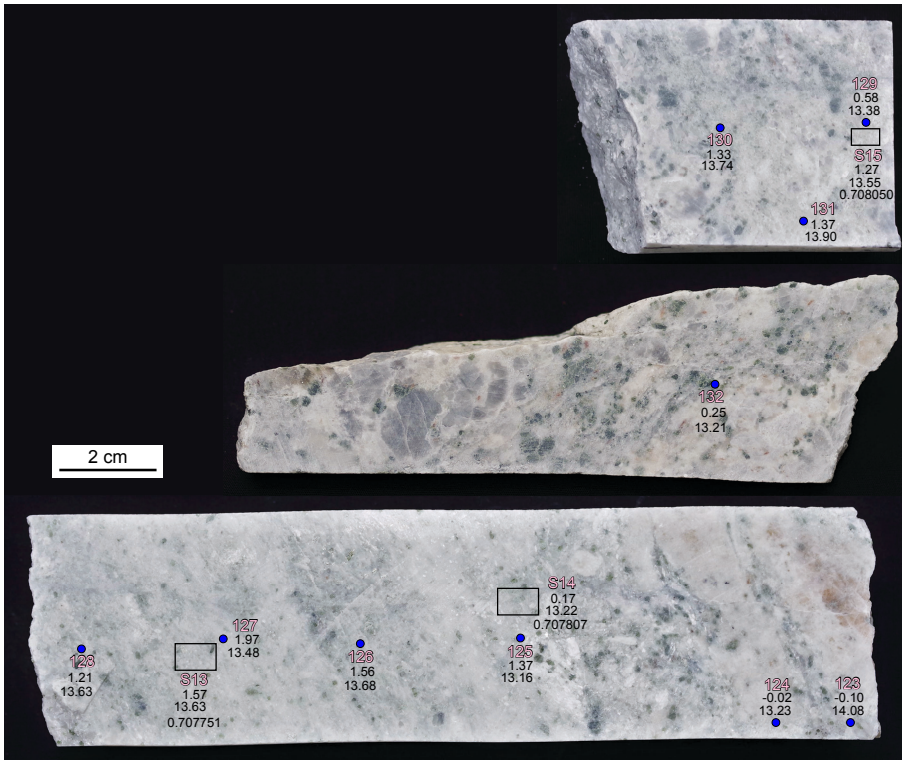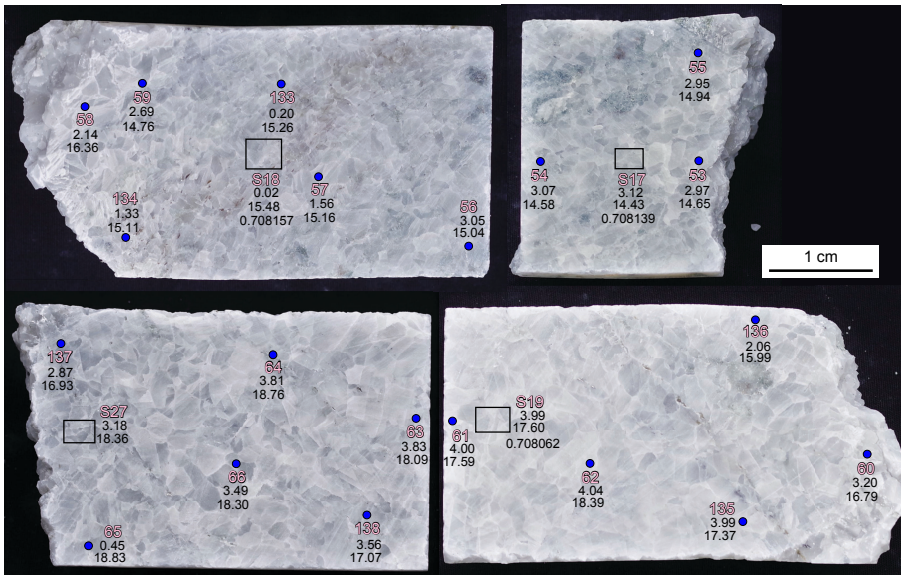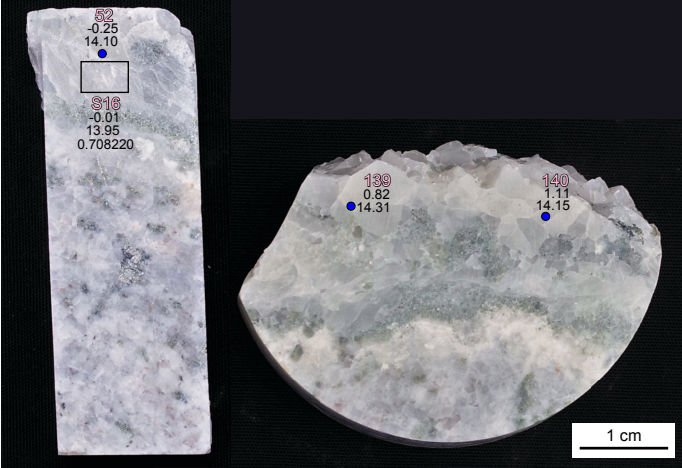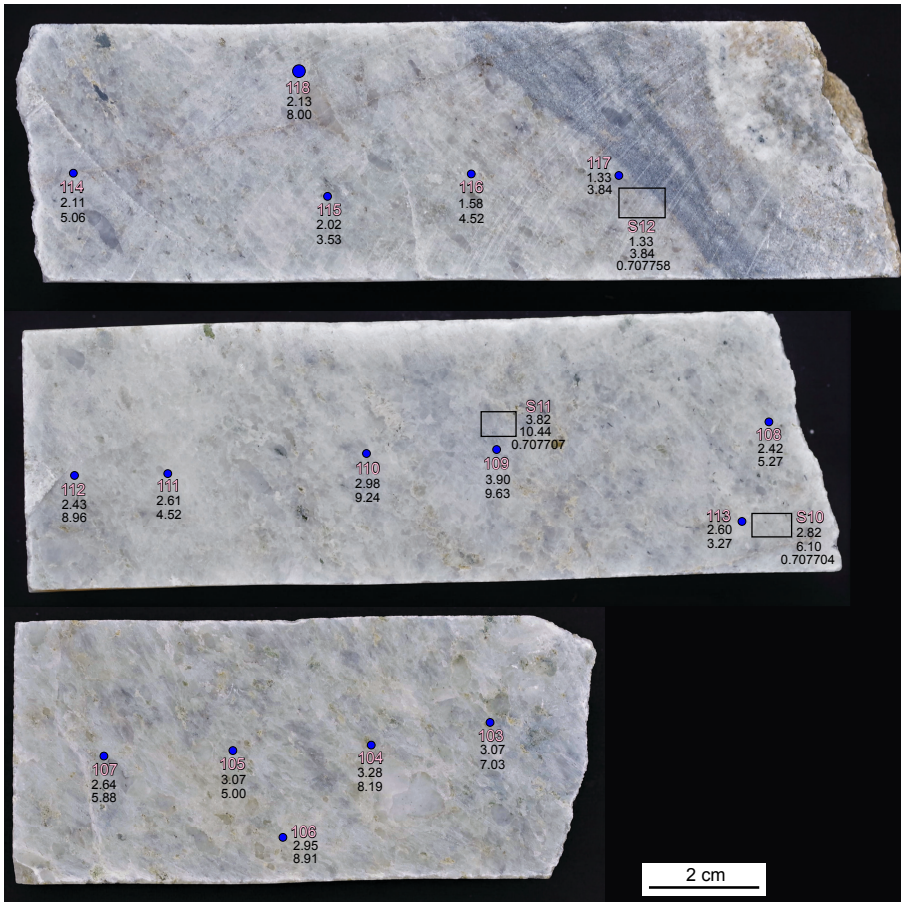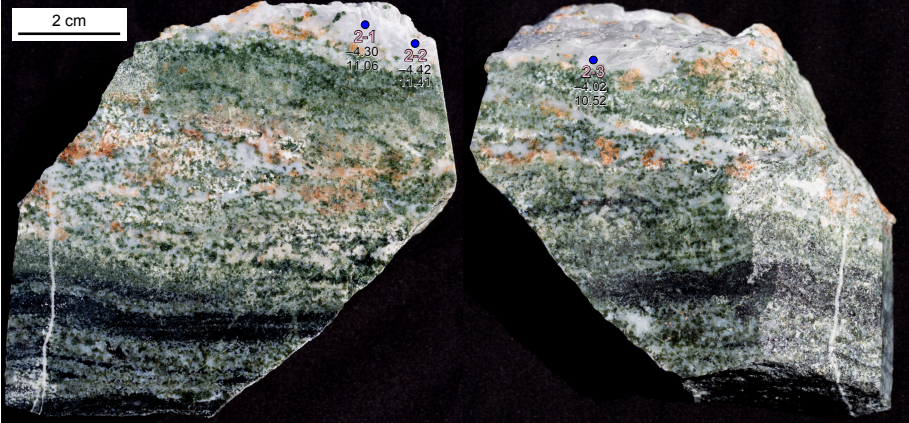
FIGURE S8

FIGURE S9

FIGURE S10
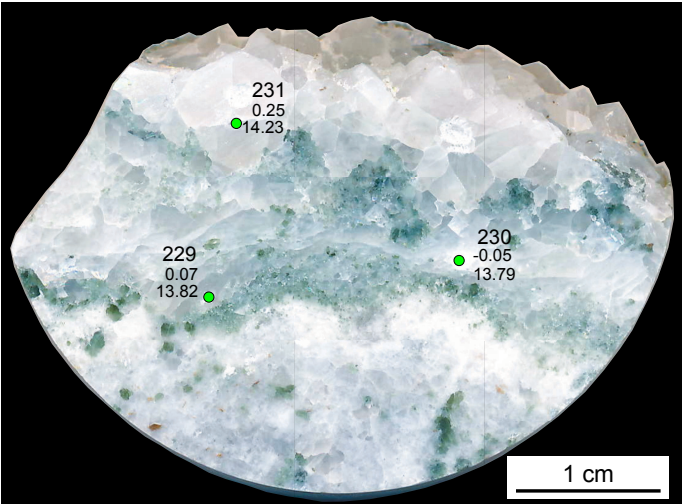
FIGURE S11

FIGURE S12

FIGURE S13

239
-3.86
9.61

228
-3.90
10.35

227
-3.95
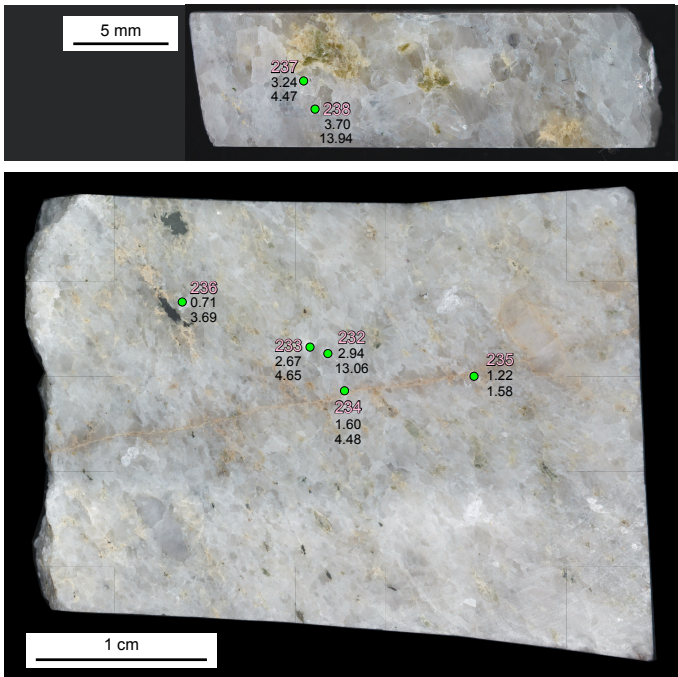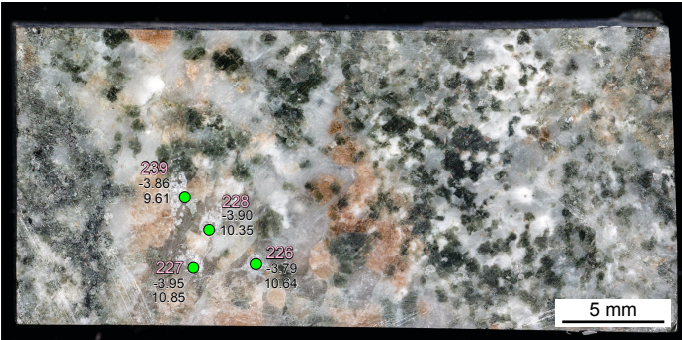10.85

226
-3.79
10.64

5 mm
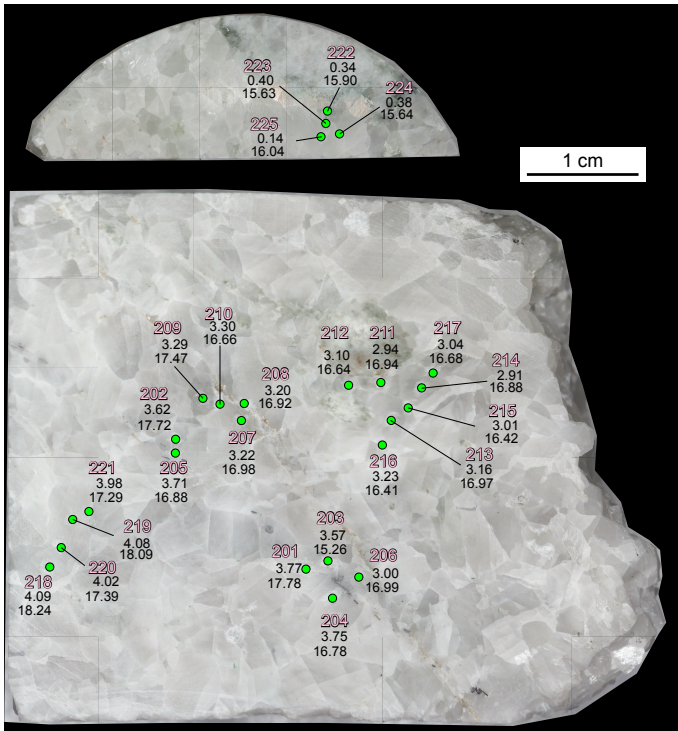
Table S1:

	Type 1			Type 2						Type 3			Type 4			Type 5		
Sample	45EANG-1-647M			1MAHI-1-575M			1MAHI-1-584.6M			1MAHI-1-582.0M			57HA-2-501.5M			KK-HD-XAXB		
No.	1[a] (core)	2[a]	3[a] (rim)	1	2	3	1	2	3	1	2	1	2[a]	3[a]	4[a]	1[a]	2[a]	3[a]
wt%																		
SiO_2	54.47	53.05	52.13	53.10	53.05	53.33	53.73	55.06	55.14	52.83	52.86	55.17	51.20	51.29	54.42	51.56	52.47	51.22
TiO_2	—	0.12	0.06	—	—	—	0.01	0.01	0.02	0.02	0.03	0.05	—	—	—	—	—	—
Al_2O_3	0.67	1.18	0.96	0.42	0.41	0.41	0.26	0.33	0.37	0.12	0.53	1.01	—	0.32	1.07	0.64	0.36	0.78
Cr_2O_3	0.15	—	0.06	0.06	—	0.05	—	0.03	—	—	—	0.00	—	—	—	—	—	—
FeO*	2.60	7.42	11.21	12.54	11.33	11.10	9.25	6.27	4.10	14.92	14.14	2.88	17.12	14.24	3.04	17.32	14.27	16.49
MnO	0.00	0.17	0.31	0.18	0.25	0.21	0.30	0.13	0.06	0.28	0.27	0.12	1.92	3.26	0.47	—	0.23	0.61
MgO	16.70	13.21	10.99	10.10	10.99	11.10	12.50	14.02	15.50	8.79	9.07	15.68	5.89	6.64	15.43	7.20	9.43	8.14
CaO	25.34	24.74	24.18	23.84	23.54	23.76	23.92	24.08	24.71	23.41	23.31	24.21	23.87	24.22	25.20	23.28	23.04	22.77
Na_2O	0.07	0.10	0.10	0.32	0.43	0.34	0.09	0.17	0.16	0.08	0.18	0.47	—	0.03	0.37	—	0.20	—
K_2O	—	0.01	—	0.05	0.09	0.05	—	—	—	0.01	—	0.08	—	—	—	—	—	—
Total	100.00	100.00	100.00	100.60	100.08	100.35	100.05	100.09	100.05	100.44	100.38	99.68	100.00	100.00	100.00	100.00	100.00	100.00
O=	6	6	6	6	6	6	6	6	6	6	6	6	6	6	6	6	6	6
Si	1.986	1.977	1.978	2.009	2.007	2.009	2.012	2.027	2.015	2.021	2.015	2.012	2.012	2.002	1.990	2.004	2.010	1.987
Ti	0.000	0.003	0.002	—	—	—	0.000	0.000	0.001	0.000	0.001	0.001	—	—	—	—	—	—
Al	0.029	0.052	0.043	0.019	0.018	0.018	0.011	0.014	0.016	0.005	0.024	0.044	—	0.015	0.046	0.029	0.016	0.036
Cr	0.004	—	0.002	0.002	—	0.001	—	0.001	—	—	—	0.000	—	—	—	—	—	—
Fe^{2+}	0.079	0.231	0.356	0.397	0.358	0.350	0.290	0.193	0.125	0.477	0.451	0.088	0.563	0.465	0.093	0.563	0.457	0.535
Mn	—	0.005	0.010	0.006	0.008	0.007	0.009	0.004	0.002	0.009	0.009	0.004	0.064	0.108	0.015	—	0.008	0.020
Mg	0.907	0.734	0.621	0.570	0.620	0.624	0.698	0.769	0.844	0.501	0.515	0.852	0.345	0.386	0.841	0.417	0.538	0.471
Ca	0.990	0.988	0.983	0.966	0.954	0.959	0.959	0.950	0.967	0.959	0.952	0.946	1.005	1.013	0.988	0.969	0.946	0.946
Na	0.005	0.007	0.007	0.023	0.031	0.024	0.006	0.012	0.011	0.006	0.013	0.034	—	0.002	0.026	—	0.015	—
K	—	0.000	0.000	0.003	0.004	0.002	—	—	—	0.001	—	0.004	—	—	—	—	—	—
Total	4.000	3.998	4.002	3.994	4.001	3.995	3.986	3.971	3.982	3.979	3.979	3.984	3.988	3.992	4.000	3.982	3.989	3.995
Mg #	0.92	0.76	0.64	0.59	0.63	0.64	0.71	0.80	0.87	0.51	0.53	0.91	0.38	0.45	0.90	0.43	0.54	0.47